

THE ROLE OF MILLISECOND PULSARS IN CONSTRAINING  
BLACK HOLE POPULATIONS IN GLOBULAR CLUSTERS:  
NEW INSIGHTS FROM MOCK DATA

by

Noha Hoque

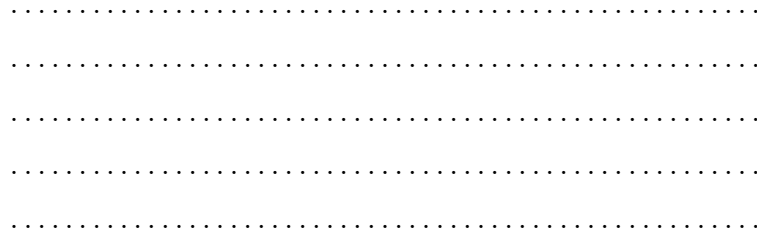
A THESIS SUBMITTED IN PARTIAL FULFILMENT OF  
THE REQUIREMENTS FOR THE DEGREE OF

BACHELOR OF SCIENCE

in

Honours Astrophysics

(Department of Astronomy and Physics, Dr. Vincent Hénault-Brunet supervising  
faculty)



SAINT MARY'S UNIVERSITY

April 30, 2025

© Noha Hoque, 2025

## ABSTRACT

Millisecond pulsars (MSPs) are rapidly rotating neutron stars with extremely stable spin periods, which can be used to analyze the central dynamics and mass distribution of globular clusters (GCs). This thesis discusses generating mock MSP data within a simulated GC and integrating multimass equilibrium dynamical models with pulsar timing data along with traditional observables to analyze the mass distribution and remnant populations in GCs. The simulated MSP observations are drawn from a selected Cluster Monte Carlo (CMC) model, with pulsar positions sampled based on the distribution of neutron stars. By analyzing the contributions from the GC's gravitational potential to MSP spin and orbital period derivatives, we aim to quantify how pulsar timing observations can influence the precision and accuracy of inferred populations of stellar-mass black holes (BHs) at the cluster core. We include different realizations of mock datasets with an increasing number of pulsars in the core of the cluster in a simulated GC. As the number of pulsars in the mock dataset increases, the population of black holes (BHs) becomes better constrained and uncertainties are more reliable. Using 25 mock pulsar realizations, we constrain the mass fraction of BHs in the cluster to 0.61%-0.90%, with reduced uncertainty. This range is closely aligned with the value derived from the CMC snapshot (0.89%), demonstrating the consistency of the process. We also investigated the real globular cluster M62 with its pulsar timing

data, where we fit multimass models under different assumptions about the cluster's heliocentric distance, evaluating fits both with and without pulsar data. The results are compared to assess how effectively pulsar timing data constrain the BH population in the cluster. Given the large number of new pulsars expected to be discovered in GCs with upcoming radio telescopes and surveys, our tests with fitting dynamical models to data that includes pulsar timing measurements for constraining BH populations in GCs will help future studies of GCs.

# Contents

<b>Contents</b> . . . . .	iv
<b>List of Figures</b> . . . . .	vi
<b>List of Tables</b> . . . . .	viii
<b>1 Introduction</b> . . . . .	1
1.1 GLOBULAR CLUSTERS . . . . .	1
1.2 MILLISECOND PULSARS . . . . .	3
1.3 PULSAR TIMING AND CLUSTER POTENTIAL . . . . .	5
1.4 MODELING GLOBULAR CLUSTERS . . . . .	9
1.5 ABOUT THIS THESIS . . . . .	12
<b>2 Generating Mock Pulsar Timing Observations</b> . . . . .	15
2.1 CLUSTER MODEL SELECTION . . . . .	15
2.2 SPIN PERIODS AND PERIOD DERIVATIVES . . . . .	17
2.3 ORBITAL PERIODS AND PERIOD DERIVATIVES . . . . .	21
2.4 VALIDATION . . . . .	22
<b>3 Fitting models to mock data</b> . . . . .	24
3.1 MODEL PARAMETERS AND PRIORS . . . . .	24

3.2 FITTING PROCESS . . . . .	26
3.3 POSTERIOR PROBABILITY DISTRIBUTIONS . . . . .	29
<b>4 Inferred black hole populations for different mock pulsar datasets</b>	<b>39</b>
<b>5 Mass models of the globular cluster M62</b>	<b>45</b>
5.1 INTRODUCTION TO M62 . . . . .	45
5.2 MODEL FITS AND COMPARISON . . . . .	47
5.3 BLACK HOLE POPULATION IN M62 . . . . .	51
<b>6 Conclusions</b>	<b>56</b>
<b>A M62 Pulsar Timing Data</b>	<b>59</b>
<b>B Fits of the mock dataset with no pulsars CMC6402-NoPulsars</b>	<b>60</b>
<b>Bibliography</b>	<b>61</b>

# List of Figures

1.1	The globular cluster M79 . . . . .	2
1.2	Schematic representation a pulsar's magnetic field lines . . . . .	4
1.3	The geometry of a pulsar's position relative to the cluster's core . . . . .	7
2.1	Gaussian KDE of the $\dot{P}$ vs. $P$ distribution of Galactic field pulsars . .	18
2.2	Pulsar sample distribution over-plotted on the KDE . . . . .	18
2.3	Mock pulsars with $P_{\text{ac}}$ component as a function of projected radius .	20
2.4	Mock pulsars with $\frac{\dot{P}}{P}$ and $\frac{\dot{P}_b}{P_b}$ as a function of projected radius . . . . .	22
3.1	2D projections of the posterior probability distributions of all model parameters for the fit to CMC6402-10PULSARS1. . . . .	30
3.2	Best-fitting model (in orange) for the CMC6402-10PULSARS3 fit . .	31
3.3	Best-fitting model (in orange) for the CMC6402-10PULSARS4 fit . .	32
3.4	Minimum and maximum values of allowed $\frac{\dot{P}}{P}$ of CMC6402-10PULSARS3 and CMC6402-10PULSARS4 . . . . .	33
3.5	Model local stellar mass functions fit to the mock observations . . . . .	33
4.1	Comparison of the posterior probability distribution of mass fraction in BHs for the fits to different mock datasets . . . . .	41

4.2	Minimum and maximum values of allowed $\frac{\dot{P}}{P}$ of CMC6402-25PULSARS6 and CMC6402-25PULSARS4 . . . . .	41
4.3	Posterior probability distribution for the mass fractions of BHs . . . . .	42
4.4	The $f_{\text{BH}}$ values inferred based on the mock observations with different sets of pulsars . . . . .	43
5.1	Best-fitting model for the M62UNIFORM-NoPULSARS fit and different datasets. . . . .	47
5.2	Best-fitting model (in orange) for the M62UNIFORM-WITHPULSARS fit and different datasets (in blue). . . . .	48
5.3	Best-fitting model for the M62GAUSSIAN-WITHPULSARS fit . . . . .	50
5.4	Minimum and maximum values of allowed $\frac{\dot{P}}{P}$ of M62UNIFORM-WITHPULSARS and M62GAUSSIAN-WITHPULSARS . . . . .	51
5.5	2D joint posterior probability distributions for seven key parameters from different fits of M62. . . . .	52
5.6	Minimum and maximum values of allowed $\frac{\dot{P}}{P}$ of M62-ONLYPULSARS	53
5.7	Best-fitting model (in orange) for the M62-ONLYPULSARS fit and dif- ferent datasets (in blue). . . . .	54
5.8	Posterior probability distribution of the mass in BHs in M62UNIFORM- WITHPULSARS in blue and M62UNIFORM-NoPULSARS in orange. .	54
5.9	Mass fraction of BHs from M62 Fits . . . . .	55

# List of Tables

3.1	Parameter Priors . . . . .	26
3.2	Summary of all mock datasets and their naming conventions. . . . .	35
3.3	Best-fitting parameters with $1\sigma$ uncertainties for fits to different realizations of the mock dataset including 5 pulsars (5.1–5.5). . . . .	36
3.4	Best-fitting parameters with $1\sigma$ uncertainties for fits to different realizations of the mock dataset including 5 pulsars (5.6–5.9). . . . .	36
3.5	Best-fitting parameters with $1\sigma$ uncertainties for (10.1–10.5). . . . .	37
3.6	Best-fitting parameters with $1\sigma$ uncertainties for models 10.6–10.10. .	37
3.7	Best-fitting parameters with $1\sigma$ uncertainties for (25.1–25.5). . . . .	38
3.8	Best-fitting parameters with $1\sigma$ uncertainties for (25.6–25.10). . . . .	38
4.1	Mock datasets with inferred BH mass fraction and BH mass . . . . .	40
5.1	Different model fits with pulsars and distance priors. . . . .	46
5.2	Medians and $1\sigma$ uncertainties of each model parameter for all five fits of M62 is shown. The naming convention of datasets and priors combination are taken from Table 5.1. . . . .	49
5.3	Total numbers in BHs for different fits of M62 and $1\sigma$ uncertainties. .	55

A.1 Pulsar timing parameters with uncertainties for pulsars M62 A, C, D, and E . . . . .	59
A.2 Timing solutions for pulsars F, G, H, and I in M62. . . . .	59
B.1 Best-fitting parameters with $1\sigma$ uncertainty for CMC6402-NoPULSARS.	60

# Chapter 1

## Introduction

### 1.1 GLOBULAR CLUSTERS

Globular clusters (GCs) are dense and spherical collections of old stars with total masses ranging from  $10^4$  to  $10^6 M_\odot$ , which are held together by gravitational forces. GCs exist in all types of galaxies, from small dwarf galaxies to massive elliptical (e.g. [Brodie and Strader, 2006](#)). All the stars in a given cluster share a common origin as they were formed from the same initial cloud of gas (e.g. [Gratton et al., 2019](#)). With ages ranging from about 10 to 13 billion years (e.g. [Forbes et al., 2018](#)), GCs are among the oldest objects in the universe. GCs are typically found in the halos of their host galaxies and their formation predominantly occurred before the majority of stellar formation in galaxies.

Being among the most luminous objects observable in galaxies, GCs provide critical insight into the conditions and processes that influenced galaxy formation and chemical evolution in the early universe ([Dotter et al., 2011; Renzini, 2017](#)). GCs are generally believed to form as single stellar populations (to a good approximation<sup>1</sup>) originating from a common gas cloud, evolving over time along predicted isochrones depending on their age, metallicity, and initial mass function ([Bastian and Lardo,](#)

---

<sup>1</sup>As stars have no significant age spread, we ignore the multiple population phenomenon that leads to star-by-star variations in light-element abundances.

2015; Binney and Merrifield, 1998).



Figure 1.1: The globular cluster M79. Image credit: ESA/Hubble.

The dense cores of GCs, as illustrated in Figure 1.1, contain tens of thousands of stars and are governed by dynamics driven primarily by stellar interactions. There are additional influences such as the host galaxy's gravitational potential and stellar mass loss. The evolutionary behaviour of these clusters is largely dictated by two-body relaxation, which leads to processes like mass segregation. During mass segregation, heavier objects gravitate toward the centre, while lighter stars move outward as their kinetic energies tend towards equilibrium or equipartition (e.g. Heggie and Hut, 2003). Consequently, the core regions become enriched with more massive stars and heavier stellar remnants compared to the outskirts. The dense environments of GCs also provide ideal conditions for the formation of black hole binaries. These black hole binaries are considered possible progenitors of many gravitational wave sources observed by detectors like LIGO and Virgo (e.g. Antonini and Gieles, 2020). The formation and retention of these black holes significantly impact the overall dynamics of the cluster, especially in the central regions where mass segregation leads to their concentration (Mackey et al., 2008; Kremer et al., 2019, e.g.). It is therefore

important to understand and quantify the populations of black holes retained in GCs.

## 1.2 MILLISECOND PULSARS

GCs contain stellar remnants such as white dwarfs, neutron stars (including millisecond pulsars, a particular type of neutron star) and stellar-mass black holes (BHs). Neutron stars in clusters can form either when accretion-induced collapse of white dwarfs exceeds the Chandrasekhar limit or from the retention of neutron stars which are born from massive star core collapses ([Grindlay and Bailyn, 1988](#)). Pulsars are rapidly rotating neutron stars, which can be formed from the collapsed cores of massive stars that have exploded in a supernova or from mass accretion onto neutron stars. These objects emit coherent radio waves along their magnetic axes. The conservation of angular momentum during the formation of the pulsar causes it to spin rapidly. When the rotation axis and the magnetic axis are misaligned, the pulsar emits pulses of radiation at time intervals corresponding to its spin period. Figure 1.2 illustrates a schematic representation of a pulsar's magnetic field lines and rotation axis.

Millisecond pulsars are a class of pulsars characterized by short periods, rapid rotation, extremely low spin-down rates, and a high likelihood of being in binary systems. The first discovery of MSPs occurred when B1937 + 21 revealed a new subclass of rapidly rotating pulsars with periods of only a few milliseconds ([Backer et al., 1982](#)). These characteristics suggest that MSPs follow a different evolutionary path compared to normal pulsars, specifically forming in an evolving binary system

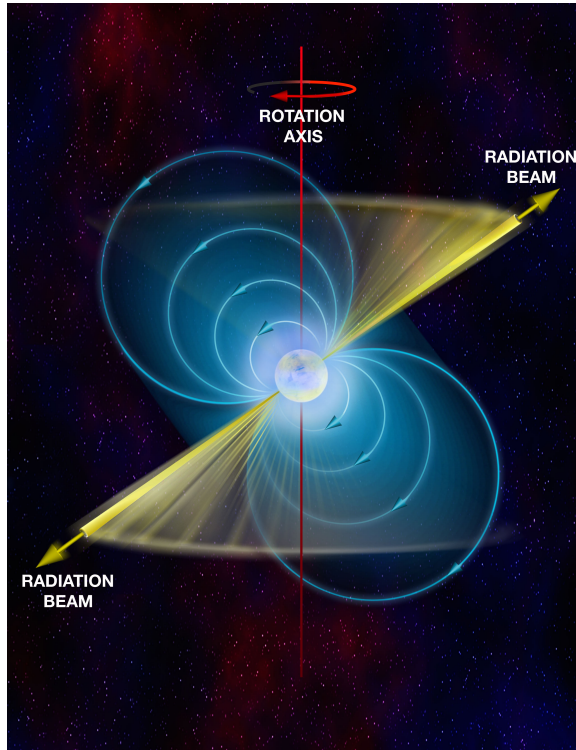


Figure 1.2: Schematic representation a pulsar. Credit: Bill Saxton; NRAO/AUI/NSF

and undergoing spin-up due to accretion from a companion star ([Alpar and Shaham, 1985](#)). The process of MSPs forming involves the companion filling its Roche lobe through transferring mass to the pulsar, which increases its angular momentum and weakens its magnetic field to about  $B \sim 10^8$  G. This reduced magnetic field minimizes energy loss through rotation. Thus, it leads to stable rotation rates (  $\dot{P} \sim 10^{-20}$  s/s ) and spin-down timescales that exceed the age of the universe. Since the discovery of the first pulsar in a GC, numerous MSPs have been identified in these clusters and the majority of them are in binary systems. A recycled pulsar is a neutron star that has been spun up by accretion from a companion, restoring rapid rotation after an initial slowdown ([Srinivasan, 2010](#)). The highly stable periods make MSPs excellent tools for probing a variety of astrophysical phenomena (e.g. [Manchester, 2017](#)).

GCs are rich sites for the production of recycled pulsars and create significantly more MSPs per unit mass compared to the galactic disk. During the past decades, 345 pulsars have been discovered in 45 Milky Way GCs<sup>2</sup> and several thousand more are predicted to exist in these systems but remain undetected (Bagchi, 2013; Freire, 2010). GCs are ancient stellar systems, where most “normal” pulsars have stopped emitting long ago and evolved into inactive neutron stars. Early work by Phinney and Hansen (1993) explored how the surrounding of a pulsar influences its observed spin-period derivative  $\dot{P}$  and, for binary pulsars, its orbital-period derivative  $\dot{P}_b$ . These studies demonstrated the potential of pulsars in GCs as powerful tools for probing cluster dynamics, which is discussed in more detail in the next section.

### 1.3 PULSAR TIMING AND CLUSTER POTENTIAL

When a pulsar moves through the gravitational field of a GC, the pulse intervals measured by a distant observer are affected by Doppler acceleration. Additionally, since the cluster itself traverses the Galactic gravitational field, the timing model for the pulses can be decomposed to reveal information about the pulsar’s intrinsic spin-down, proper motion, Galactic potential, and—central to this thesis, the gravitational potential of the cluster in which the pulsar resides (e.g. Prager et al., 2017). MSPs’ remarkably stable spin periods make pulsars ideal probes, as any observed changes in their periods—beyond the intrinsic spin-down caused by magnetic braking—can be largely attributed to external influences. We can also measure the orbital period

---

<sup>2</sup><https://www3.mpifr-bonn.mpg.de/staff/pfreire/GCpsr.html>

derivative of GC pulsars in binary systems. The orbital periods of these binaries are typically on the order of days, but their intrinsic rate of change (e.g. due to the emission of gravitational waves) is extremely small, so observed changes in orbital periods can be directly related to the gravitational acceleration of the pulsar in the cluster potential, Galactic potential and pulsar's proper motion. Thus, we can gain valuable insights into the gravitational potential of the pulsar's host cluster using MSPs (e.g. Prager et al., 2017; Smith et al., 2024).

To establish a consistent reference framework for the line-of-sight acceleration of pulsars, we define a coordinate system for a GC, as illustrated in Figure 1.3. The plane passing through the cluster's centre of gravity (CoG) and oriented perpendicular to our line of sight (LOS) is denoted as  $O$ , representing the plane of the sky. The projected distance of each pulsar from the CoG on this plane is referred to as  $R_{\perp}$ . The core radius,  $r_c$ , is defined as the distance where the cluster's mass density decreases to one-third of its central value. Additional key radii include the half-mass radius ( $r_h$ ) and the tidal radius ( $r_t$ ) of the cluster.

The LOS position perpendicular to the plane  $O$  is denoted as  $l$ . Positions  $l_1$  and  $l_2$  shown on Figure 1.3 represent two possible locations along the LOS within the cluster where the same observed line-of-sight acceleration  $a_l$  can occur. The maximum LOS acceleration at a given  $R_{\perp}$  is represented by  $a_{\max}(R_{\perp})$ . When the pulsar is at  $l=0$ , the acceleration component along the LOS is zero. The LOS component of the acceleration vector is increasing along the LOS as a pulsar moves away from plane  $O$ , up to a distance approximately equal to the core radius  $r_c$ . The gravitational acceleration also weakens as a pulsar moves away from the centre of the mass distribution. As a

result, the LOS acceleration peaks at some intermediate distance (from plane  $O$ ) and then decreases along the LOS.

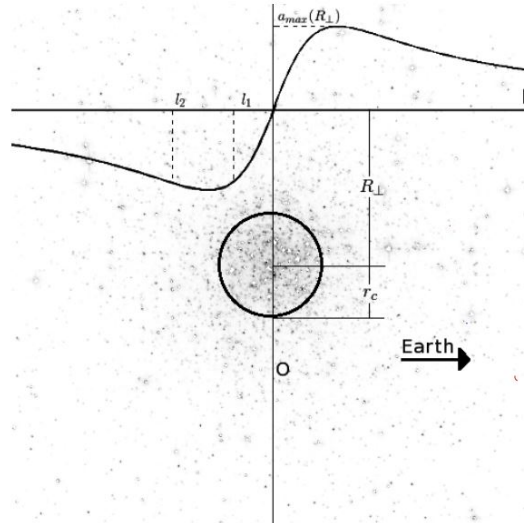


Figure 1.3: The geometry of a pulsar’s position relative to the cluster’s core is depicted, with the core radius highlighted and the line-of-sight acceleration overlaid on an optical image of Terzan 5, captured by the Hubble Space Telescope. For a measured line-of-sight acceleration less than  $a_{l,\max}(R_\perp)$ , there are two possible line-of-sight positions, marked  $l_1$  and  $l_2$ , corresponding to the same acceleration value. See the main text for a description of the coordinate system shown here. Diagram from [Prager et al. \(2017\)](#).

We outline our approach for using pulsar timing data to infer acceleration. This process follows a relationship between changes in a pulsar’s spin and orbital periods and the acceleration it experiences ([Phinney and Hansen, 1993](#)). For a pulsar situated within a smooth, spherically symmetric potential, the observed variation in its spin period results from a combination of its intrinsic spin-down and any additional acceleration along the line of sight. These contributions can be expressed as:

$$\left(\frac{\dot{P}}{P}\right)_{\text{obs}} = \left(\frac{\dot{P}}{P}\right)_{\text{int}} + \frac{a_{\text{cl},z}}{c} + \frac{a_G}{c} + \frac{a_S}{c} + \frac{a_{\text{DM}}}{c}, \quad (1.1)$$

where the observed period derivative  $\left(\frac{\dot{P}}{P}\right)_{\text{obs}}$  is decomposed into distinct components.

In the equation  $c$  is speed of light. The components include the pulsar's intrinsic spin-down rate,  $\left(\frac{\dot{P}}{P}\right)_{\text{int}}$ , primarily influenced by magnetic braking, and contributions from the following sources:

- $a_{\text{cl},z}$ : The LOS acceleration due to the cluster's gravitational potential, which is crucial to constrain the internal mass distribution of the cluster. This term divided by  $c$  gives  $P_{\text{ac}}$ , the cluster potential component.
- $a_G$ : The acceleration along the line of sight caused by the gravitational potential of the Milky Way. This term divided by  $c$  gives us the Galactic potential component  $P_{\text{ag}}$ .
- $a_s$ : The apparent acceleration from the Shklovskii effect ([Shklovskii, 1970](#)), resulting from the pulsar's proper motion. This term divided by  $c$  gives us proper motion component  $P_s$ .
- $a_{\text{DM}}$ : Changes in the dispersion measure (DM) caused by variations in the interstellar medium between the pulsar and the observer.

The effects of the cluster's proper motion and the Galaxy's gravitational potential are relatively well constrained based on the pulsar's position and motion in the Galaxy ([Baumgardt and Vasiliev, 2021](#)). However, intrinsic processes such as magnetic braking require careful analysis to consider their contribution to the observed period derivative. This decomposition provides a framework for isolating and studying the cluster's gravitational potential through pulsar timing measurements ([Prager](#)

et al., 2017; Smith et al., 2024).

The spin-period derivative  $\dot{P}$  and orbital-period derivative  $\dot{P}_b$  of MSPs in GCs constrain the gravitational potential of their host clusters particularly in regions where crowding and extinction hinder the acquisition of detailed stellar kinematic data, the more traditional probe of cluster potential (Smith et al., 2024). Recent studies have used MSP data to conduct detailed analyses of the gravitational potentials of GCs. Notable examples include Terzan 5 (Prager et al., 2017; Smith et al., 2024), 47 Tuc (Freire et al., 2017; Abbate et al., 2018; Smith et al., 2024), NGC 6752 (Corongiu et al., 2006), NGC 6624 (Gieles et al., 2017), M62 (Abbate et al., 2019) and NGC 5139 (Bañares-Hernández et al., 2025). We will summarize the results of some these studies in the next section.

## 1.4 MODELING GLOBULAR CLUSTERS

Recent research has made significant use of pulsar timing data in GCs to explore various aspects of astrophysics in constraining dark remnants in GCs (Smith et al., 2024; Wang and Xie, 2021). Some examples of such works for 47 Tuc, NGC 6624, M62 and NGC 6752 are discussed below. Freire et al. (2017) presented a single-mass King model for 47 Tuc, based on over 20 years of timing data for 23 pulsars and had precise measurements of their spin and orbital periods and period derivatives. By analyzing spin period derivatives and orbital period changes, the authors constrained the cluster's gravitational potential and found no evidence of an intermediate-mass black hole (IMBH) at its center. Instead, the observed pulsar period derivatives

and jerks (the second time derivative of periods) within the core of the cluster were consistent with the King model assuming cluster distance of 4.69 kpc. [Hénault-Brunet et al. \(2020\)](#) reached similar conclusions with a multimass model, not a single-mass King model (i.e. no evidence for an IMBH).

[Perera et al. \(2017\)](#) presents proof for an IMBH in the globular cluster NGC 6624. [Gieles et al. \(2017\)](#) developed multimass models of the cluster NGC 6624 that successfully explain the surface brightness profile, proper motion kinematics from HST, and the stellar mass function at various distances from the centre of the cluster without requiring an IMBH. They analyzed the observed spin period derivative of one pulsar in NGC 6624 and compared it to multimass models but did not directly fit these models to the pulsar data. They show that the high acceleration inferred from the pulsar's period derivative can be explained by the cluster stellar mass distribution, which includes dark remnants such as neutron stars and white dwarfs. Additionally, they argue that the previously reported evidence of an IMBH based on higher-order period derivatives, is instead caused by passing stars and stellar remnants rather than an IMBH. They also show that NGC 6624 may be a core-collapsed cluster, which would be inconsistent with the presence of an IMBH.

In NGC 6752 [Corongiu et al. \(2006\)](#) showed that from the five pulsar timing measurements, the period derivatives and inferred accelerations favoured the presence of a non-luminous mass of at least  $2.56 \times 10^4 M_{\odot}$  in the core of the cluster.

M62 has 10 binary pulsars with precise timing solutions for spin period and period derivatives for all of them and orbital period and period derivatives for 5 of them ([Vleeschower et al., 2024](#)). In this thesis, we show how that can help us to constrain

dark remnants in the cluster core using multimass dynamical models along with the pulsar data.

The dynamics of GCs are generally modelled using two primary approaches. The first, called “evolutionary models” involves simulating the entire cluster’s evolution, often through direct N-body integration (e.g. Baumgardt, 2017) or Monte Carlo methods (e.g. Rodriguez et al., 2022; Giersz et al., 2013), based on the method by Hénon (1971). While these models offer valuable insights into cluster dynamics, they are computationally expensive, with even optimized versions requiring several days of computation for a realistic cluster (Rodriguez et al., 2022). The second approach is the “equilibrium models”, which focuses exclusively on present-day cluster conditions. These models include the LIMEPY family (Gieles and Zocchi, 2015). They can explore a wider range of parameters than evolutionary models. They can be used along statistical techniques such as MCMC and Nested Sampling when fitting models to data. Nested sampling is a Bayesian algorithm that estimates model evidence and posterior distributions by progressively sampling from smaller regions of the prior that have increasingly higher likelihood. Equilibrium models offer more flexibility compared to evolutionary models, as they are less computationally demanding and enable variations in parameters such as the stellar mass function and remnant retention fractions. LIMEPY models capture the different spatial distribution and kinematics of objects of different masses due to mass segregation in clusters and have been validated through comparisons with N-body simulations (Peuten et al., 2016). LIMEPY models can successfully describe the mass distribution in GCs, as demonstrated in mock data tests (Hénault-Brunet et al., 2019) and applications to real

Milky Way clusters (Hénault-Brunet et al., 2020). Moreover, multimass models of 34 Milky Way GCs by Dickson et al. (2023, 2024) show that stellar-mass black hole populations typically account for less than 1% of cluster mass, with the exception of Omega Centauri with more than 5% of the cluster mass in BHs. Smith et al. (2024) have introduced new self-consistent multimass models for 47 Tuc and Terzan 5. They fitted models to traditional observables including velocity dispersion profiles, number density profiles, and local stellar mass functions along with pulsar timing data. The models make use of updated stellar mass functions (Baumgardt et al., 2023), Gaia distance constraints (Baumgardt and Vasiliev, 2021), and modern stellar evolution prescriptions to properly constrain potential stellar-mass black hole populations. For 47 Tuc, the strong constraints on its overall mass distribution favour a small population of stellar-mass black holes of approximately  $446 M_{\odot}$  and the model can explain all the data considered without needing to invoke an IMBH. Terzan 5 contains the highest number of MSPs among Milky Way GCs but has limited kinematic data. Considering pulsar timing data which helped Smith et al. (2024) significantly improve existing estimates of its mass distribution and set an upper limit of around  $4000 M_{\odot}$  for its black hole population. Thus, we can conclude that pulsar timing data can serve as a powerful tool for investigating the dynamics of GCs for which we have limited conventional stellar kinematic data.

## 1.5 ABOUT THIS THESIS

Dickson et al. (2023, 2024) used multiple observables to constrain both the total and

visible mass components with multimass models, effectively mapping the distribution of dark mass within Milky Way GCs. This was demonstrated by fitting the models to data (including mock observations extracted from snapshots of Monte Carlo simulations) but without using any pulsar timing information. Later, [Smith et al. \(2024\)](#) integrated multimass equilibrium dynamical models with pulsar timing data (along with traditional observables) to analyze the mass distribution and remnant populations in the globular clusters 47 Tuc and Terzan 5.

My research builds upon these works where I repeat similar experiments as in [Dickson et al. \(2024\)](#). However, now I include mock pulsar data to assess the true uncertainties on the recovered mass fraction in BHs when considering pulsar timing observations in the multimass model fitting procedure. I start with generating mock pulsar data with periods and period derivatives (spin and orbital) within a simulated cluster. Then I combine the pulsar mock data with other mock observations (velocity dispersion profile, number density profile, stellar mass functions), and fit multimass models to these mock data in the same way models would be fitted to real data. By fitting dynamical models to these mock observations and pulsar timing data, I aim to assess the precision and accuracy of constraints on black hole populations obtained by fitting dynamical models to the data that includes pulsar timing measurements. The remainder of this thesis is structured as follows:

Chapter 2 describes the detailed methodology used to generate mock pulsars with timing solutions within the cluster. I sample their positions by analyzing snapshots from Cluster Monte Carlo (CMC) models and generate mock pulsar observations by sampling spin and orbital period derivatives with uncertainties, accounting for various

contributing factors. Chapter 3 presents the results of fitting multimass models under different assumptions about the MSP population. Fits to different realizations of the mock datasets are analyzed to assess sampling effects and statistical variations in the results.

Chapter 4 explores the inferred black hole fraction obtained from fitting mock observations and compares it to the true black hole fraction. This chapter also evaluates the reliability of these constraints in characterizing black hole populations in GCs. Chapter 5 focuses on the analysis of the GC M62. We fit multimass models under different assumptions about the cluster’s heliocentric distance, evaluating fits both with and without pulsar data, and using only pulsar data. The results are compared through visualizations to assess how effectively pulsar timing data constrain the black hole population in the cluster. Chapter 6 summarizes the conclusions of this work and outlines potential directions for future research, including further refinements of mock data and extensions to other clusters.

# Chapter 2

# Generating Mock Pulsar Timing Observations

## 2.1 CLUSTER MODEL SELECTION

To create the mock pulsar samples with period derivative measurements, we first need to select a globular cluster model containing neutron stars. For this, we chose a snapshot from the existing grid of the Cluster Monte Carlo (CMC) catalogue<sup>1</sup>, as mentioned earlier. CMC is a Monte Carlo code for stellar dynamics based on Hénon’s method (Hénon, 1971), which simulates the evolution of globular clusters under the assumption of spherical symmetry. The CMC simulations track the dynamical evolution of globular clusters over a Hubble time, showing the effects of dynamical interactions on the formation and evolution of different stellar populations (Kremer et al., 2020). The CMC cluster catalogue results from these simulations, varying four initial cluster parameters: the initial number of particles, virial radius, Galactocentric distance, and metallicity.

Throughout the entire lifetime of the cluster, the simulations produce snapshots at different times. Each of the snapshots provides information on stellar types (e.g. main sequence stars, white dwarfs, BHs, neutron stars, etc.), radial positions, velocities and

---

<sup>1</sup><https://cmc.ciera.northwestern.edu/>

physical properties (e.g. mass, luminosity, etc.) of all cluster objects. These snapshots can be used to construct surface brightness or number density profiles and velocity dispersion profiles, as demonstrated in previous studies and also stellar mass function observations (Dickson et al., 2024). For example, Rui et al. (2021) created simulated surface brightness and velocity dispersion profiles from each CMC model snapshot to compare them with corresponding observed profiles of GCs. Using these simulated profiles, they fitted dynamical models from the CMC cluster catalog to 59 Milky Way GCs.

For this thesis, we select the snapshot N1.6e6-rv1-rg2-Z0.0002 (we will refer to it as CMC 6402 or CMC snapshot) which satisfactorily matches the observations (velocity dispersion and surface brightness profile) of NGC 6402 (M14). We sample pulsars based on the properties of this snapshot. The reason behind choosing this particular snapshot is the cluster is massive ( $4.2 \times 10^5 M_{\odot}$ ) at present day (age 10.007 Gyr) and still contains 258 BHs and a total mass in BHs of  $2471.71 M_{\odot}$ . Our model fitting works more reliably for clusters with a higher central mass concentration, which results in a larger maximum line-of-sight acceleration of pulsars near the cluster centre, as discussed thoroughly in Chapter 3. To analyze the selected snapshot, we used CMCTOOLKIT, a Python package for analyzing CMC star cluster simulations (Pattabiraman et al., 2013; Rui et al., 2021). 500 mock pulsars were sampled based on the radial distribution of neutron stars in the snapshot. Since we need observed periods and period derivatives for both spin and orbital periods, we generated the components that contribute to pulsar spin and orbital  $\left(\frac{\dot{P}}{P}\right)_{\text{obs}}$  from the observer's perspective, as given in Equation 1.1.

## 2.2 SPIN PERIODS AND PERIOD DERIVATIVES

We start with generating spin period measurements for the mock pulsars. The intrinsic period derivative component  $(\frac{\dot{P}}{P})_{\text{int}}$  appears from processes such as magnetic braking or active accretion. Since we assume that none of the pulsars are accreting, the intrinsic period change was attributed solely to magnetic braking, making  $(\frac{\dot{P}}{P})_{\text{int}}$  positive in the mock samples. The intrinsic spin-down is assumed to depend only on the pulsar spin period, as  $(\frac{\dot{P}}{P})_{\text{int}}$  is randomly drawn from the same distribution as Galactic field pulsars as shown in Figure 2.1. We make a distribution of possible  $\dot{P}$  values with respect to  $P$  values using Galactic field pulsars from the ATNF pulsar catalogue<sup>2</sup> as a reference to build a distribution of possible values  $(\frac{\dot{P}}{P})_{\text{int}}$  to sample from (Figure 2.2).

An uncertainty of  $2 \times 10^{-16}$  s, mimicking real pulsar data in the globular cluster M62, is used as error for  $P$ . We sample the noise contribution from a Gaussian with this error as the standard deviation, and then add it to the previously generated spin period  $P$ . We use an uncertainty of  $3 \times 10^{-25}$  s for  $\dot{P}$  values based on pulsar data in M62 and sample the noise contribution in a similar way. By dividing  $\dot{P}$  values by  $P$ , we obtain the intrinsic spin-down component  $(\frac{\dot{P}}{P})_{\text{int}}$ .

The  $P_{\text{ac}}$  component in equation 1.1 represents period variations due to the cluster's gravitational potential. Originating from Doppler shifts, this acceleration term is a result of evaluating the rate of change of the pulsar's period, caused by acceleration due to the internal mass distribution of the cluster. Using the mock pulsar samples,

---

<sup>2</sup><https://www.atnf.csiro.au/research/pulsar/psrcat/>

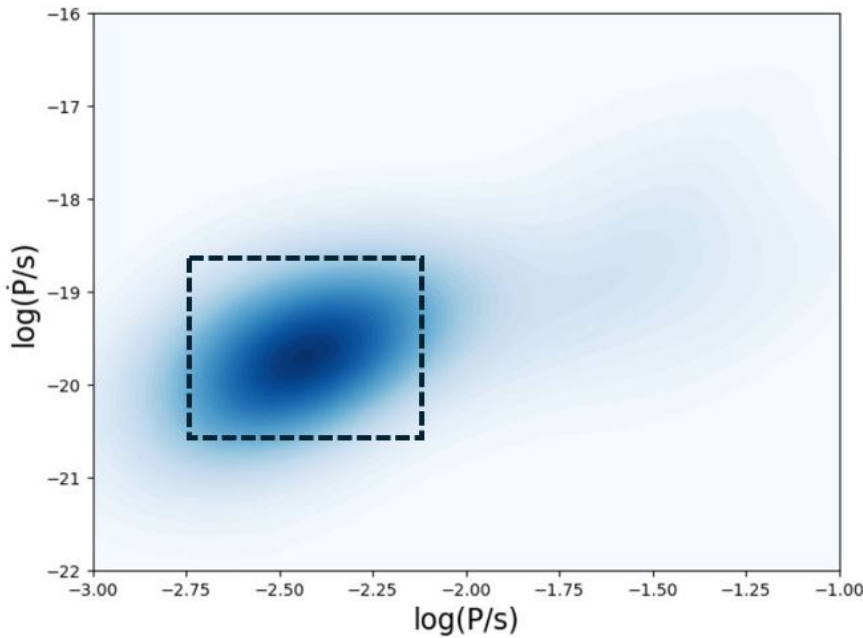


Figure 2.1: Gaussian KDE (in blue) of the  $\dot{P}$  vs.  $P$  distribution of Galactic field pulsars. The rectangle represents the millisecond pulsar regime and the part of the distribution from which we sample values for  $\left(\frac{\dot{P}}{P}\right)_{\text{int}}$ . Darker colours represent regions of higher probability density.

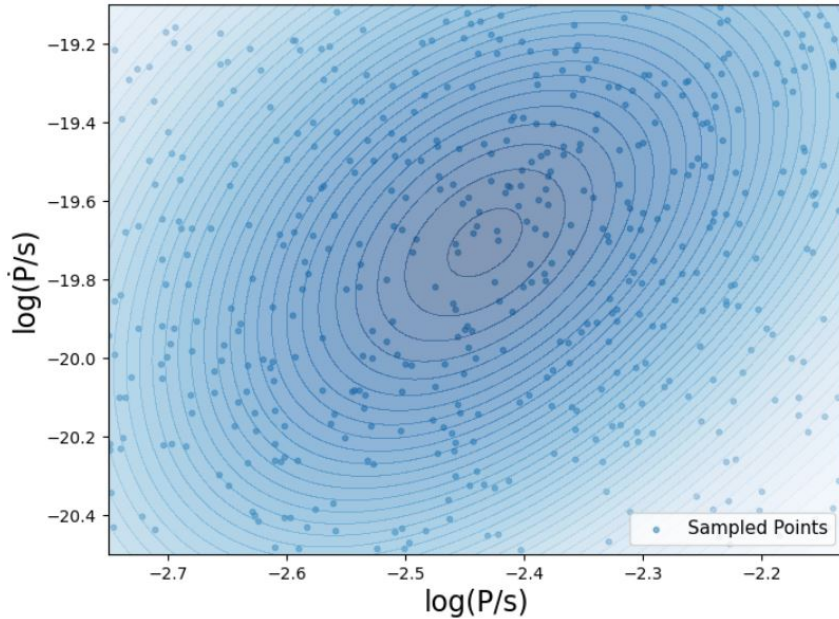


Figure 2.2: The random pulsar samples distribution obtained from the Gaussian KDE of the  $\frac{\dot{P}}{P}$  distribution.

we obtain their 3D distances from the cluster centre  $r$  and the cumulative mass of the cluster at the 3D distance from the centre of each mock pulsar. From the 3D radial distance, we sample the LOS position of the pulsars with the  $z$ -coordinates.  $z$ -coordinates are randomly sampled assuming a random distribution of spherical angles  $\theta$  and  $\phi$ . The  $z$ -coordinates are determined by  $r \cos \theta$ , where  $\theta$  is uniformly sampled between 0 and 1 in order to get random orientation (or random sampling on a sphere). The  $P_{\text{ac}}$  component is evaluated using the following equation:

$$a_{\text{cl},z} = \frac{GM_{(<r)}z}{r^3}, \quad (2.1)$$

where  $a_{\text{cl},z}$  is the line-of-sight acceleration,  $G$  is the gravitational constant,  $M_{(<r)}$  is the cumulative mass within radius  $r$  as mentioned above, the  $z$  coordinate is described above in Figure 1.3 as  $l$  and  $r$  is the 3D distance from the cluster centre of the pulsars.

Equation 2.1 is used to calculate the LOS acceleration, which is then divided by  $c$  to obtain  $P_{\text{ac}}$ . We plot distribution of LOS accelerations (effectively the  $P_{\text{ac}}$  component of  $\dot{\vec{P}}$ ) for all sampled pulsars as a function of their projected radius in Figure 2.3. Figure 2.3 also shows the maximum and minimum allowed  $\dot{\vec{P}}$  values due to the cluster potential a function of projected radius. These contours trace the cluster's mass distribution, where the mass density near the centre is dominated by heavy remnants due to mass segregation. As a result, towards the centre of the cluster, the maximum acceleration increases. This plot will be used as reference again in later sections. In this particular plot, all the mock pulsar samples are plotted with their  $P_{\text{ac}}$  component only. This also shows how the pulsars trace the maximum acceleration

contours perfectly (i.e. they are all contained within the envelope).

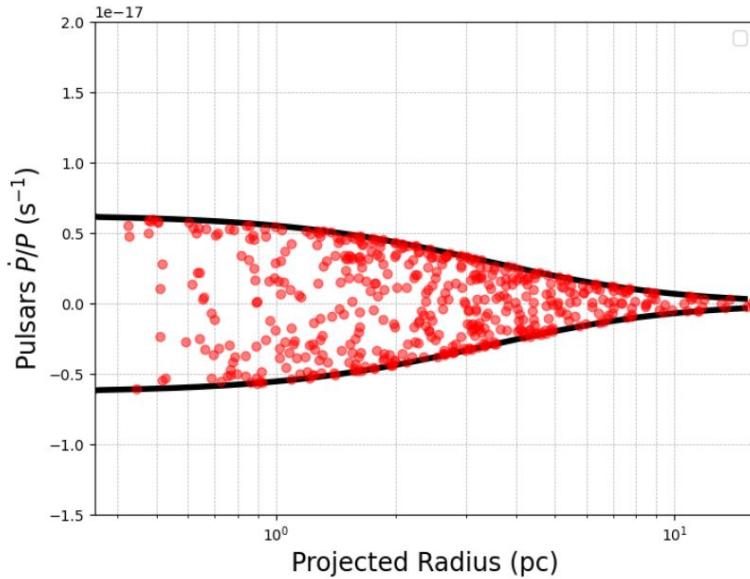


Figure 2.3: Minimum and maximum values of allowed  $\frac{\dot{P}}{P}$  due to the cluster potential are traced by the black solid lines. The mock pulsars with  $P_{ac}$  component as a function of projected radius are shown with red circles.

The additional period derivative components due to the cluster's proper motion ( $P_s$ ) and the Galactic potential ( $P_{ag}$ ) depend on the cluster's position and motion in the galaxy. Both components can be calculated directly using GCFIT<sup>3</sup> (presented by [Dickson et al. 2023, 2024](#) and explained in chapter 3). We adopted the galactic position and distance from NGC 6402, the cluster this snapshot resembles. The Galactic contribution to  $\frac{\dot{P}}{P}$ , denoted as  $P_{ag}$ , accounts for acceleration along the line of sight due to the Milky Way's gravitational potential. The mass distribution of the Galaxy and the cluster's (and pulsars') position within the Galaxy are required for this calculation, with GCFIT using the MilkyWayPotential2022 model from GALA ([Price-Whelan et al., 2017](#)). The proper motion contribution  $P_s$  arises from the Shklovskii

<sup>3</sup><https://github.com/nmdickson/GCfit/>

effect (Shklovskii, 1970), where pulsars display apparent line-of-sight acceleration due to their transverse motion. This component is computed using GCFIT with inputs of cluster proper motion and distance.

Variations in  $\dot{P}/P$  due to dispersion measure fluctuations between the pulsar and observer are not considered for these samples. All the above-mentioned spin period derivative components,  $(\frac{\dot{P}}{P})_{\text{int}}$ ,  $P_{\text{ac}}$ ,  $P_s$  and  $P_{ag}$  are combined to obtain the observed  $(\frac{\dot{P}}{P})_{\text{obs}}$ .

## 2.3 ORBITAL PERIODS AND PERIOD DERIVATIVES

We generate orbital periods  $P_b$  and period derivatives  $\dot{P}_b$  for all mock pulsars, assuming they are in binary systems. However, we only use the orbital period derivatives for a fraction of them when fitting models to mock data, assuming some pulsars are single stars. In binary pulsars, orbital period variations are entirely caused by the cluster potential, Galactic potential, and proper motion contributions. Any intrinsic orbital period change would occur on a much longer timescale as mentioned previously and not lead to a significant contribution to the observed orbital period derivative. To compute the observed  $\frac{\dot{P}_b}{P_b}$ , we use Equation 1.1 again, this time excluding the intrinsic component of period derivative, and combine the mock pulsar data accordingly. The orbital period  $P_b$  was set to  $1.15 \times 10^4$  s, based on an M62 pulsar. The specific choice of  $P_b$  value does not affect the analysis, as we only need it to compute the uncertainty contributions to  $\frac{\dot{P}_b}{P_b}$  but the ratio  $\frac{\dot{P}_b}{P_b}$  is dictated by the cluster potential and not the properties of the binaries.

The adopted uncertainties associated with the spin period  $P$  and spin period derivative  $\dot{P}$  for mock pulsars were referenced from real M62 pulsars. These uncertainties were used as standard deviations of Gaussian noise distributions when we create mock period and period derivative measurements. For  $P_b$ , uncertainties were taken from the same pulsar's orbital solution, while for  $\dot{P}_b$ , uncertainties were assumed to be of the same magnitude as  $\dot{P}_b$  values, based on the ratio of  $P_b$  to  $\dot{P}_b$  in M62 pulsars.

## 2.4 VALIDATION

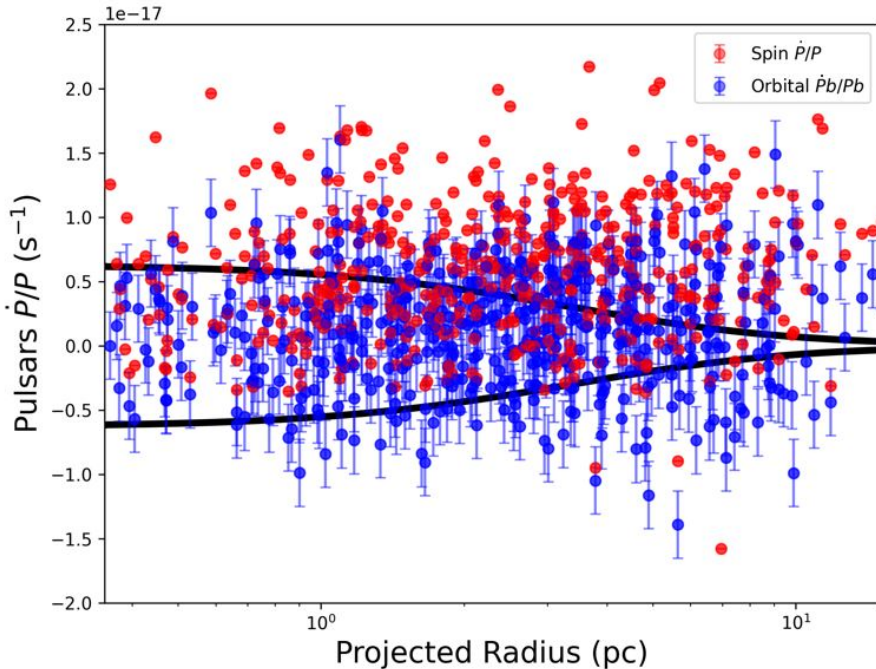


Figure 2.4: Minimum and maximum values of allowed  $\frac{\dot{P}}{P}$  of mock pulsars are traced by the black solid lines. The mock pulsars as a function of projected radius with spin  $\frac{\dot{P}}{P}$  and  $\frac{\dot{P}_b}{P_b}$  are shown with red circles and blue circles respectively.

Figure 2.4 shows the minimum and maximum allowed  $\dot{P}/P$  due to the cluster

potential, as was previously shown in Figure 2.3. In Figure 2.4, the  $\dot{P}/P$  of the mock pulsars (calculated from Equation 1.1) is plotted as a function of projected radius, for both spin and orbital periods and period derivatives. As we add all components, we see the spin period derivatives are biased towards the positive side due to the contribution from intrinsic spin down. The dataset of 500 mock pulsars, containing their projected radii (in arc minutes), spin periods, spin period derivatives, orbital periods, orbital period derivatives and their associated uncertainties, is hereby ready for model fitting. However, as any given cluster would have much fewer than 500 pulsars, we do not include them all at once. We created this larger sample of mock pulsars to be able to randomly select different subsamples of pulsars (different realisations of a pulsar dataset) from this large mock dataset.

# Chapter 3

## Fitting models to mock data

### 3.1 MODEL PARAMETERS AND PRIORS

LIMEPY multimass distribution-function (DF) based models are used to model the spatial distribution of GCs. DF based models uses Poisson's equation to solve for the system's potential and describe the particle density of stars (and phase-space distribution) that satisfies the collisionless-Boltzmann equation ([Gieles and Zocchi, 2015](#)). These calculate the mass distribution and velocity distribution of objects (as a function of their mass) for a system in equilibrium. [Dickson et al. \(2023, 2024\)](#) presented the GCFIT package, which combines LIMEPY with an algorithm to compute the evolution of stars as a function of mass and creates mass bins for use in the multimass model (including realistic remnant mass functions). GCFIT can also fit models to a number of provided observables by computing the likelihood of the data given the model parameters, and taking into account prior probability distributions. Posterior samples for the model parameters can be obtained with the nested sampling procedure from the DYNESTY software package ([Speagle, 2020](#)). It can also use a Markov Chain Monte Carlo (MCMC) procedure, but we are using the nested sampling algorithm for this work. In this thesis, we use GCFIT when we sample pulsars and also for model fitting to explore the dynamics and mass distribution of GCs (using

both mock GC observations in this chapter and chapter 4, and real observations of the M62 cluster in Chapter 5).

To compute a model there are 13 free parameters used: (1) dimensionless central potential parameter  $W_0$ , capturing the concentration of the cluster, (2) truncation parameter  $g$  (mimicking the effect of galactic tides), (3) total cluster mass  $M$  and (4) 3D half-mass radius  $r_h$ , (5) anisotropy radius parameter  $r_a$ , controlling the amount of radial velocity anisotropy, (6) mass-dependent velocity scale  $\delta$ , to capture the effect of mass segregation, (7) number density nuisance parameter  $s^2$  (capturing unaccounted uncertainties in the number density profile fit), (8) mass function nuisance parameter  $F$  (capturing inaccuracies in the mass function assumed), (9,10,11) the slopes  $\alpha_1$ ,  $\alpha_2$ , and  $\alpha_3$  of a three-segment broken power law which define the initial mass function used for generating input mass bins, (12) black hole retention fraction  $\text{BH}_{\text{ret}}$ , which sets the percentage of the mass in BHs, initially created from massive star progenitors that is retained in the cluster at the present day after natal kicks and dynamical ejections and (13)  $d$ , the heliocentric distance to the GC. When fitting a model, the adopted priors on the parameters above are uniform for most parameters and for the bounds we consider a wide reasonable range suitable for each parameter as displayed in Table 3.1. The heliocentric distance prior is taken as a Gaussian distribution based on the measurements and uncertainty of [Baumgardt and Vasiliev \(2021\)](#). The priors on the mass function power-law slopes are taken from [Dickson et al. \(2023\)](#).

Parameter	Distribution	Range/Values
$W_0$	Uniform	[2.0, 10.0]
$M[10^6 M_\odot]$	Uniform	[0.05, 1.3]
$r_h[\text{pc}]$	Uniform	[0.0, 12.0]
$\delta$	Uniform	[0.3, 0.5]
$s^2$	Uniform	[0.0, 15.0]
$F$	Uniform	[1.0, 7.5]
$a_1$	Uniform	[-1.0, 2.35]
$a_2$	Uniform	[-1.0, 2.35], [ $a_1$ , 4.0]
$a_3$	Uniform	[1.6, 4.0], [ $a_2$ , 4.0]
$\text{BH}_{\text{ret}}[\%]$	Uniform	[0.0, 50.0]
$d[kpc]$	Gaussian	9.14, $\sigma = 1$

Table 3.1: Model parameters and their priors for the fits to mock cluster CMC6402. Uniform priors bound all parameters except distance within physically reasonable ranges. For the distance, we use a Gaussian prior with the distance measurement from [Baumgardt and Vasiliev \(2021\)](#) and its uncertainty providing the mean  $\mu$  and standard deviation  $\sigma$  of the prior. The distance for CMC6402 is 9.14 kpc. The distance priors adopted for fits of M62 are discussed in details in chapter 5.

## 3.2 FITTING PROCESS

We extract the mock observational datasets that mimick CMC snapshot. GCFIT adjusts model parameters for fitting until the model properties closely match various observations of GC structure and kinematics from the snapshot. The observations constrain the distribution of visible cluster stars and the total mass of the cluster from kinematic profiles (both line-of-sight velocity dispersion and proper motion dispersion profiles as a function of projected radius and stellar mass function data). We use mock proper motion data from the Hubble Space Telescope (HST) and *Gaia* proper motions typically available for Milky Way GCs. Moreover, the velocity anisotropy of the

cluster can be constrained using the kinematics in the radial and tangential directions in the plane of the sky. The combination of LOS velocity dispersion and proper motion dispersion profiles gives a 3D view of the cluster kinematics. For the mock datasets from the CMC snapshot, the number density profiles, LOS velocity dispersion and proper motion dispersion profiles are mock profiles, so they are computed from the snapshot. However, for M62, the projected number density (ND) radial profiles of the clusters are taken from [deBoer et al. \(2019\)](#), which is very important to constrain the spatial structure and concentration of the GC. We also use stellar mass function (MF) data of the snapshot to constrain the present-day mass function (PDMF) of the cluster, assess mass segregation, and estimate the total mass in visible stars. When fitting models to observations of M62, we compare our models with measurements of the stellar mass function from [Baumgardt et al. \(2023\)](#), which are obtained from deep HST photometry consisting of star counts and binned by stellar mass.

The models are simultaneously fitted to the data described above (PM dispersion profiles, LOS velocity dispersion profile, ND profile, stellar MF at different projected distances from the cluster centre) plus the pulsar datasets, which gives us the posterior probability distribution of the best-fitting model parameters of the cluster through Bayesian parameter estimation techniques ([Dickson et al., 2023](#)). The returned set of weighted posterior samples is used to construct posterior probability distributions for all model parameters. These samples are obtained using nested sampling as mentioned before.

To fit models to the mock pulsar  $\frac{\dot{P}}{P}$  data, we construct a likelihood function that accounts for all physical contributions to the observed period derivatives. For spin

$\frac{\dot{P}}{P}$ , we combine three key components: (1) the probability distribution for the LOS acceleration from the cluster’s gravitational potential, which depends on the model parameters; (2) the intrinsic spin-down distribution of pulsars, sampled from observed Galactic pulsar data; and (3) the measurement uncertainty, modelled as a Gaussian centred on zero with the observed error width. These components are convolved together, with additional shifts applied for the Galactic potential and Shklovskii (proper motion) effects, which are treated as known point estimates. The resulting probability distribution serves as our likelihood function, enabling Bayesian inference of the cluster parameters. For orbital  $\frac{\dot{P}_b}{P_b}$ , we follow a similar approach but exclude intrinsic contributions, as orbital period derivatives are dominated by external accelerations. While orbital derivatives have larger uncertainties, they offer independent verification of the cluster potential and are not affected by the significant spin-down component that is important for the spin-period derivatives. This comprehensive method ensures all physical effects and measurement errors are properly incorporated when evaluating model fits to the mock pulsar data.

To evaluate our modelling approach, we conducted multiple fits to mock datasets using the selected CMC snapshot with varying numbers of pulsars (5, 10, and 25), as detailed in Table 3.2 along with the traditional observational datasets. For each pulsar count, we generated several realizations of the pulsar mock dataset by randomly selecting pulsars from our comprehensive dataset of 500 mock pulsars (discussed in Chapter 2) with their spin period and period derivative measurements. We use the orbital period derivative and period for only a fraction of the pulsars as shown in the table. Additionally, we performed a baseline fit without any pulsars (CMC6402-

NoPULSARS, presented in Appendix B), which we use to evaluate the added value of including pulsars.

### 3.3 POSTERIOR PROBABILITY DISTRIBUTIONS

In the remainder of this chapter, we discuss the resulting posterior probability distributions of all model parameters along with the fits to datasets with different mock pulsar sample realizations. An example of the resulting posterior distributions for a fit to a dataset that includes 10 mock pulsars (with 5 pulsars having orbital period derivatives) is shown in Figure 3.1.

The best-fitting model is plotted along with several observables in Figure 3.2 and 3.3 for mock datasets CMC6402-10PULSARS3 and CMC6402-10PULSARS4. The reason behind choosing these particular datasets is to show the differences of model fitting. The models are fit only on the radial and tangential components of the PM separately, while the total proper motion dispersion and anisotropy ratio of the best-fitting model are shown but these quantities are not fitted. The best-fitting model for the CMC6402-10PULSARS3 mock dataset is in excellent agreement with the observational data, while it is not the same case for CMC6402-10PULSARS4, respectively. From the plots of  $\frac{\dot{P}}{P}$  in Figure 3.4, we see that a possible explanation for this discrepancy may be the distribution of the “observed” period derivatives. As more pulsars have large positive observed spin period derivatives (or  $\frac{\dot{P}}{P}$ ) in mock dataset CMC6402-10PULSARS4 the limited pulsar dataset may favour more mass in the centre, even though this leads to an overestimated central velocity dispersion when

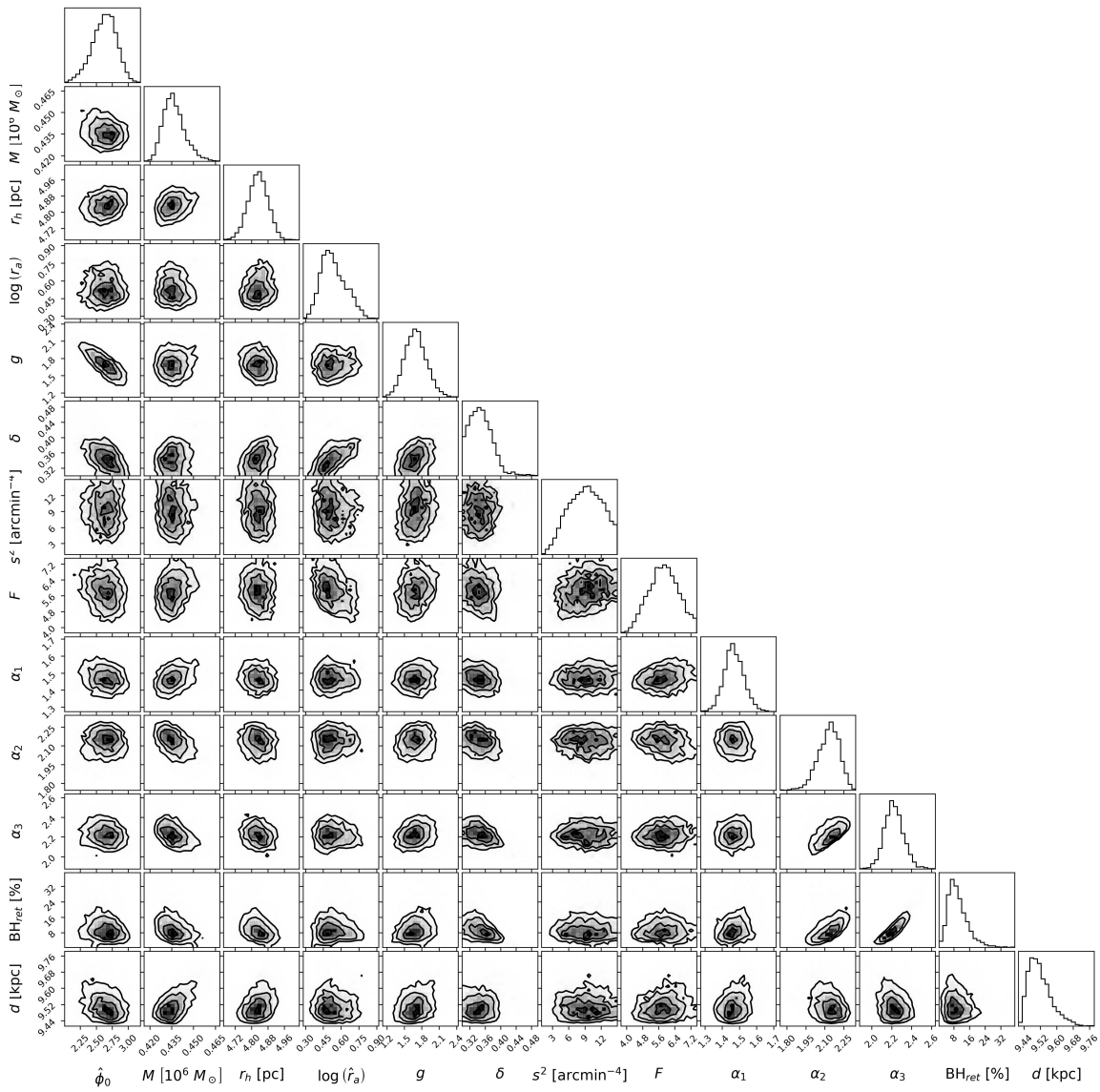


Figure 3.1: 2D projections of the posterior probability distributions of all model parameters for the fit to CMC6402-10PULSARS1.

compared to the LOS and PM dispersion datasets. In principle, the contribution from intrinsic spin-down is included in the likelihood function for the spin period derivative, so it should be taken into account without requiring more mass. We believe this is an artifact or limitation of the fitting procedure when applied to a dataset that has a limited number of pulsars but includes a few pulsars with large observed spin period derivatives.

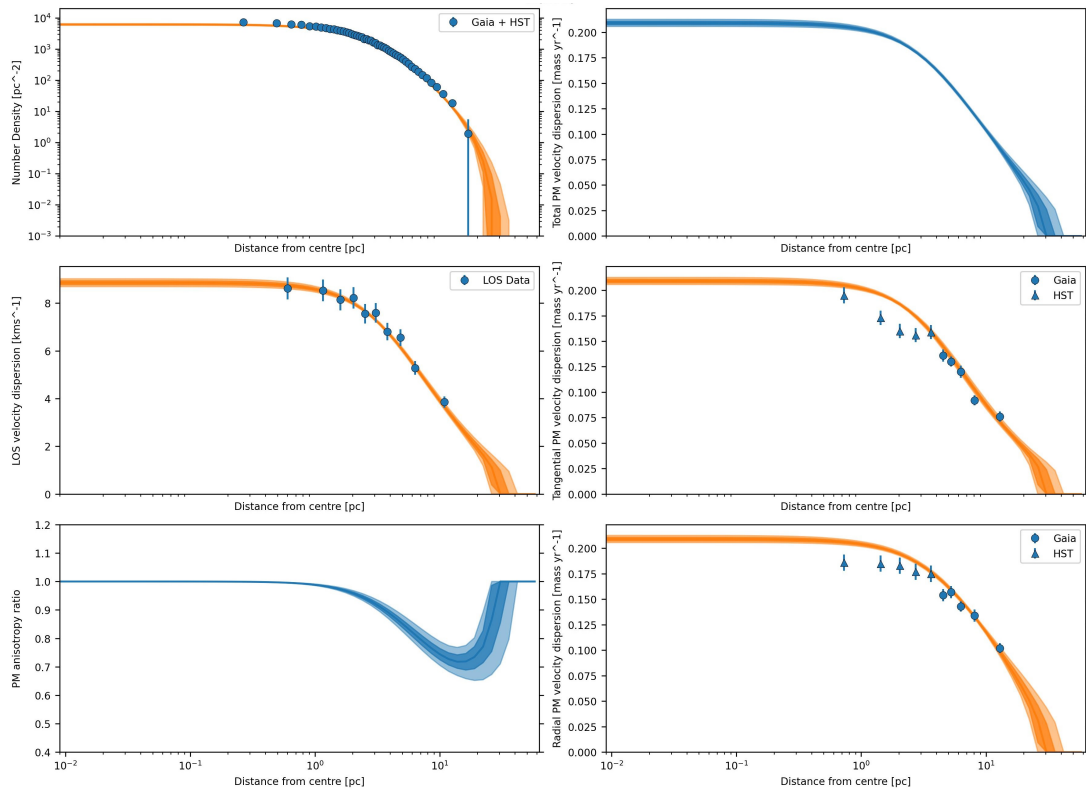


Figure 3.2: Best-fitting model (in orange) for the CMC6402-10PULSARS3 fit and different mock datasets (in blue). Top left: Model fit to the projected number density profile. Middle left: Model fit to the line-of-sight velocity dispersion profile. Bottom left: Model of the proper motion anisotropy profile. Right panels: Model of the total proper motion dispersion profile, separated into tangential (middle-right panel) and radial (bottom-right panel) components.

The stellar mass functions of the best-fitting models are shown in Figure 3.5 for CMC6402-10PULSARS3. In the best-fitting models for mass functions, the fits to mock datasets with different numbers of pulsars all match the given data almost perfectly.

The best-fitting parameters with  $1\sigma$  uncertainties for different realizations of mock datasets including 5, 10 and 25 pulsars are displayed in Table 3.3-3.8. The best-fitting models that do not agree with the observations like Figure 3.3 are hereby labelled as “bad” fits. The different realizations of mock datasets with 5 pulsars such as

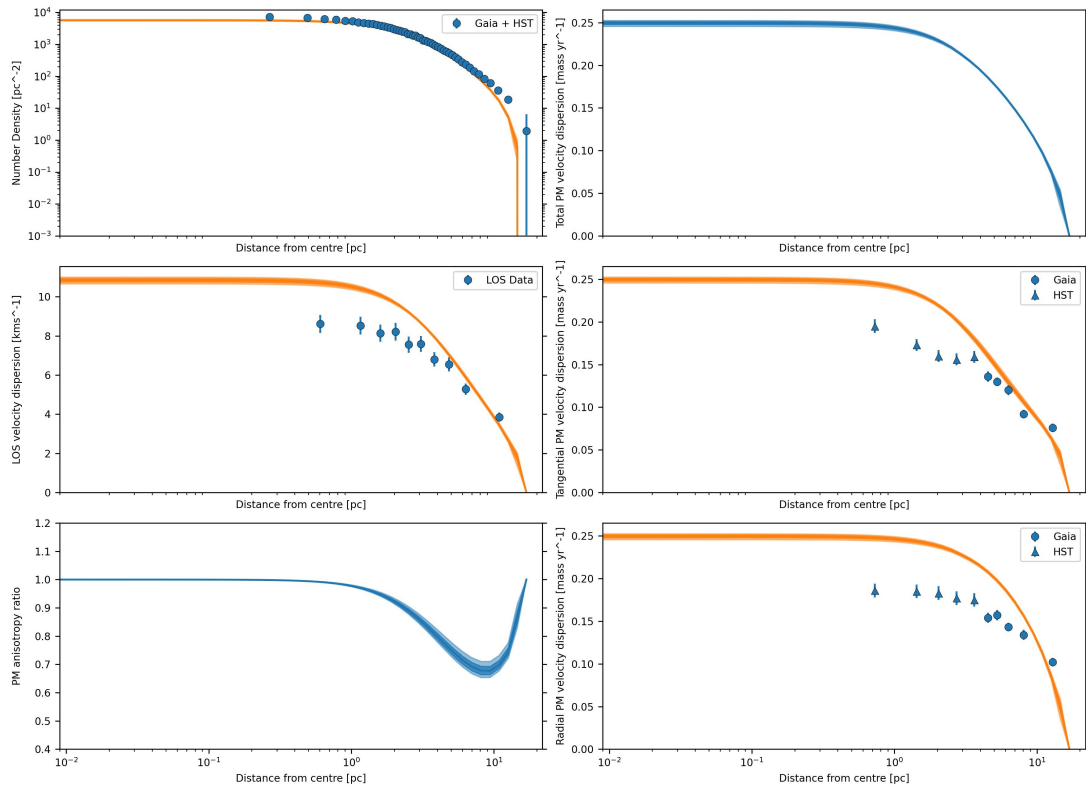


Figure 3.3: Best-fitting model (in orange) for the CMC6402-10PULSARS4 fit and different mock datasets (in blue). Top left: Model fit to the projected number density profile. Middle left: Model fit to the line-of-sight velocity dispersion profile. Bottom left: Model of the proper motion anisotropy profile. Right panels: Model of the projected total proper motion dispersion profile, separated into tangential (middle-right panel) and radial (bottom-right panel) components.

CMC6402-5PULSARS1, CMC6402-5PULSARS2 are denoted as 5.1, 5.2 and so on.

While fitting different realizations that include periods and period derivatives of 25 pulsars, it has been challenging to find models that consistently match the observational data. As previously discussed, this difficulty likely arises due to the presence of a few outlier pulsars exhibiting large positive observed spin period derivatives. To accommodate these excess pulsars, the model tends to favor a higher velocity dispersion, ultimately resulting in a bad fit overall. In contrast, the good fit models show excellent agreement with the observations, featuring narrow posterior distributions

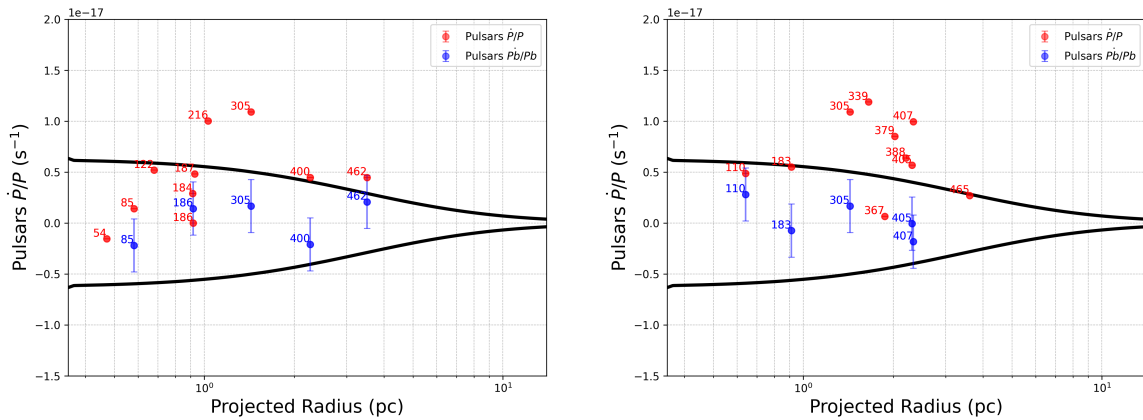


Figure 3.4: Minimum and maximum values of allowed  $\frac{\dot{P}}{P}$  due to the cluster potential as a function of projected radius for CMC6402-10PULSARS3 on the left and CMC6402-10PULSARS4 on the right. The black lines here are calculated from the underlying mass distribution in the snapshot. The dots are all the mock pulsars plotted with all components of spin  $\frac{\dot{P}}{P}$  in red and  $\frac{\dot{P}_b}{P_b}$  in blue.

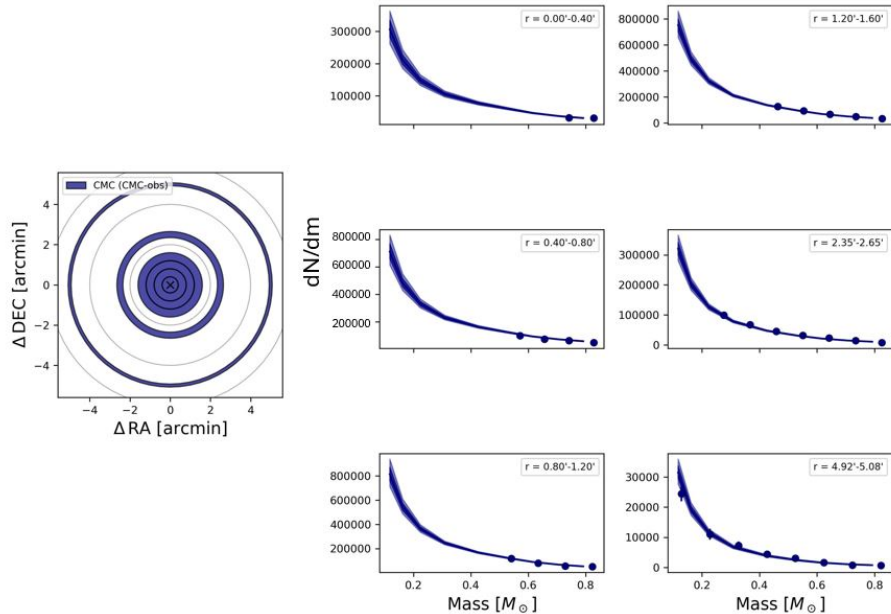


Figure 3.5: Model local stellar mass functions fit to the mock observations of CMC6402-10PULSARS3. Each panel presents the number of stars per unit mass as a function of stellar mass for different distance ranges from the centre as indicated in the legend according to the left panel. The observations used to constrain the models are shown with dots with their  $1\sigma$  uncertainties.

that closely align with the true value of the mass in BHs from the model snapshot as discussed in Chapter 4.

Name of Dataset	Total Number of Pulsars	Number of Spin $\dot{P}$	Number of Orbital $\dot{P}_b$	Naming Convention
CMC6402-5Pulsars1	5	5	3	5.1
CMC6402-5Pulsars2	5	5	3	5.2
CMC6402-5Pulsars3	5	5	3	5.3
CMC6402-5Pulsars4	5	5	3	5.4
CMC6402-5Pulsars5	5	5	3	5.5
CMC6402-5Pulsars6	5	5	3	5.6
CMC6402-5Pulsars7	5	5	3	5.7
CMC6402-5Pulsars8	5	5	3	5.8
CMC6402-5Pulsars9	5	5	3	5.9
CMC6402-10Pulsars1	10	10	5	10.1
CMC6402-10Pulsars2	10	10	5	10.2
CMC6402-10Pulsars3	10	10	5	10.3
CMC6402-10Pulsars4	10	10	5	10.4
CMC6402-10Pulsars5	10	10	5	10.5
CMC6402-10Pulsars6	10	10	5	10.6
CMC6402-10Pulsars7	10	10	5	10.7
CMC6402-10Pulsars8	10	10	5	10.8
CMC6402-10Pulsars9	10	10	5	10.9
CMC6402-10Pulsars10	10	10	5	10.10
CMC6402-25Pulsars1	25	25	12	25.1
CMC6402-25Pulsars2	25	25	12	25.2
CMC6402-25Pulsars3	25	25	12	25.3
CMC6402-25Pulsars4	25	25	12	25.4
CMC6402-25Pulsars5	25	25	12	25.5
CMC6402-25Pulsars6	25	25	12	25.6
CMC6402-25Pulsars7	25	25	12	25.7
CMC6402-25Pulsars8	25	25	12	25.8
CMC6402-25Pulsars9	25	25	12	25.9
CMC6402-25Pulsars10	25	25	12	25.10
CMC6402-NoPulsars	0	0	0	CMC6402-NoPulsars

Table 3.2: Summary of all mock datasets and their naming conventions.

Parameter	Models				
	5.1	5.2	5.3	5.4	5.5
$W_0$	$2.9_{-0.12}^{+0.12}$	$2.8_{-0.15}^{+0.14}$	$2.4_{-0.13}^{+0.12}$	$2.7_{-0.15}^{+0.14}$	$2.0_{-0.02}^{+0.07}$
$M[10^6 M_\odot]$	$0.39_{-0.01}^{+0.01}$	$0.41_{-0.01}^{+0.01}$	$0.58_{-0.01}^{+0.01}$	$0.43_{-0.01}^{+0.01}$	$0.63_{-0.01}^{+0.01}$
$r_h[\text{pc}]$	$4.8_{-0.05}^{+0.05}$	$4.8_{-0.05}^{+0.05}$	$4.9_{-0.04}^{+0.04}$	$4.8_{-0.05}^{+0.05}$	$5.0_{-0.04}^{+0.04}$
$\delta$	$0.39_{-0.03}^{+0.02}$	$0.36_{-0.03}^{+0.03}$	$0.33_{-0.02}^{+0.02}$	$0.37_{-0.03}^{+0.02}$	$0.30_{-0.01}^{+0.01}$
$s^2$	$9.0_{-4.1}^{+3.9}$	$9.3_{-3.8}^{+3.5}$	$12_{-2.3}^{+2.2}$	$12_{-2.3}^{+2.1}$	$14_{-1.3}^{+0.9}$
$F$	$4.1_{-0.5}^{+0.7}$	$4.9_{-0.6}^{+0.7}$	$7.3_{-0.2}^{+0.1}$	$5.8_{-0.7}^{+0.7}$	$7.5_{-0.1}^{+0.0}$
$a_1$	$1.2_{-0.1}^{+0.1}$	$1.3_{-0.1}^{+0.1}$	$1.8_{-0.0}^{+0.1}$	$1.4_{-0.1}^{+0.1}$	$2.0_{-0.0}^{+0.1}$
$a_2$	$2.3_{-0.1}^{+0.0}$	$2.2_{-0.1}^{+0.1}$	$1.9_{-0.0}^{+0.1}$	$2.1_{-0.1}^{+0.1}$	$2.0_{-0.0}^{+0.1}$
$a_3$	$2.4_{-0.1}^{+0.1}$	$2.3_{-0.1}^{+0.1}$	$1.9_{-0.0}^{+0.1}$	$2.2_{-0.1}^{+0.1}$	$2.0_{-0.0}^{+0.1}$
$\text{BH}_{\text{ret}}[\%]$	$9.7_{-3.6}^{+7.3}$	$10_{-3.8}^{+7.5}$	$4.1_{-1.0}^{+1.5}$	$7.2_{-3.3}^{+13}$	$12_{-1.7}^{+6.1}$
$d[\text{kpc}]$	$8.8_{-0.1}^{+0.1}$	$9.1_{-0.1}^{+0.1}$	$10.06_{-0.02}^{+0.01}$	$9.4_{-0.0}^{+0.1}$	$10.69_{-0.06}^{+0.06}$
Good Fit?	✓	✓	✓	✓	✗

Table 3.3: Best-fitting parameters with  $1\sigma$  uncertainties for fits to different realizations of the mock dataset including 5 pulsars (5.1–5.5).

Parameter	5.6	5.7	5.8	5.9
$W_0$	$2.9_{-0.11}^{+0.12}$	$2.4_{-0.22}^{+0.21}$	$2.2_{-0.16}^{+0.15}$	$2.9_{-0.12}^{+0.11}$
$M[10^6 M_\odot]$	$0.39_{-0.01}^{+0.01}$	$0.45_{-0.01}^{+0.01}$	$0.50_{-0.01}^{+0.01}$	$0.39_{-0.01}^{+0.01}$
$r_h[\text{pc}]$	$4.75_{-0.05}^{+0.04}$	$4.78_{-0.06}^{+0.06}$	$4.83_{-0.07}^{+0.08}$	$4.77_{-0.05}^{+0.05}$
$r_a$	$0.61_{-0.10}^{+0.12}$	$0.45_{-0.07}^{+0.09}$	$0.40_{-0.07}^{+0.08}$	$0.60_{-0.11}^{+0.13}$
$g$	$1.3_{-0.1}^{+0.2}$	$1.8_{-0.2}^{+0.2}$	$1.9_{-0.1}^{+0.1}$	$1.2_{-0.2}^{+0.2}$
$\delta$	$0.36_{-0.03}^{+0.03}$	$0.33_{-0.02}^{+0.03}$	$0.32_{-0.02}^{+0.03}$	$0.38_{-0.03}^{+0.03}$
$s^2$	$8.3_{-3.0}^{+3.6}$	$9.2_{-3.4}^{+3.6}$	$8.0_{-2.8}^{+3.2}$	$7.4_{-3.3}^{+4.4}$
$F$	$4.5_{-0.7}^{+0.9}$	$6.5_{-0.7}^{+0.6}$	$6.9_{-0.4}^{+0.4}$	$4.6_{-0.7}^{+0.7}$
$a_1$	$1.3_{-0.1}^{+0.1}$	$1.5_{-0.1}^{+0.1}$	$1.7_{-0.0}^{+0.0}$	$1.3_{-0.1}^{+0.1}$
$a_2$	$2.3_{-0.1}^{+0.1}$	$2.1_{-0.1}^{+0.1}$	$1.9_{-0.1}^{+0.1}$	$2.3_{-0.1}^{+0.0}$
$a_3$	$2.5_{-0.1}^{+0.1}$	$2.2_{-0.1}^{+0.1}$	$1.9_{-0.1}^{+0.1}$	$2.4_{-0.1}^{+0.1}$
$\text{BH}_{\text{ret}}[\%]$	$13_{-4.9}^{+10}$	$9.8_{-4.3}^{+6.3}$	$5.2_{-2.1}^{+5.2}$	$10_{-3.8}^{+8.3}$
$d[\text{kpc}]$	$8.96_{-0.10}^{+0.13}$	$9.62_{-0.08}^{+0.08}$	$9.99_{-0.10}^{+0.09}$	$8.93_{-0.12}^{+0.11}$
Good Fit?	✓	✓	✓	✗

Table 3.4: Best-fitting parameters with  $1\sigma$  uncertainties for fits to different realizations of the mock dataset including 5 pulsars (5.6–5.9).

Parameter	10.1	10.2	10.3	10.4	10.5
$W_0$	$2.6_{-0.2}^{+0.2}$	$2.6_{-0.2}^{+0.2}$	$2.8_{-0.1}^{+0.1}$	$2.1_{-0.0}^{+0.1}$	$2.5_{-0.1}^{+0.1}$
$M$	$0.44_{-0.01}^{+0.01}$	$0.44_{-0.01}^{+0.01}$	$0.40_{-0.00}^{+0.00}$	$0.61_{-0.00}^{+0.01}$	$0.53_{-0.00}^{+0.00}$
$r_h$	$4.8_{-0.0}^{+0.0}$	$4.8_{-0.0}^{+0.0}$	$4.5_{-0.0}^{+0.0}$	$4.6_{-0.0}^{+0.1}$	$4.7_{-0.0}^{+0.0}$
$r_a$	$0.52_{-0.09}^{+0.13}$	$0.52_{-0.09}^{+0.13}$	$0.46_{-0.07}^{+0.09}$	$0.05_{-0.03}^{+0.06}$	$0.24_{-0.05}^{+0.08}$
$\gamma$	$1.7_{-0.2}^{+0.2}$	$1.7_{-0.2}^{+0.2}$	$1.2_{-0.2}^{+0.2}$	$0.43_{-0.07}^{+0.05}$	$0.40_{-0.08}^{+0.10}$
$\delta$	$0.35_{-0.03}^{+0.03}$	$0.35_{-0.03}^{+0.03}$	$0.34_{-0.02}^{+0.03}$	$0.31_{-0.00}^{+0.01}$	$0.34_{-0.02}^{+0.03}$
$s_2$	$9.2_{-3.4}^{+3.3}$	$9.2_{-3.4}^{+3.3}$	$9.6_{-3.8}^{+3.4}$	$14.4_{-0.7}^{+0.4}$	$13.7_{-1.2}^{+0.9}$
$F$	$5.9_{-0.8}^{+0.8}$	$5.9_{-0.8}^{+0.8}$	$5.2_{-0.7}^{+0.8}$	$7.5_{-0.1}^{+0.0}$	$7.4_{-0.2}^{+0.1}$
$a_1$	$1.5_{-0.1}^{+0.1}$	$1.5_{-0.1}^{+0.1}$	$1.3_{-0.1}^{+0.0}$	$2.3_{-0.0}^{+0.0}$	$1.9_{-0.0}^{+0.0}$
$a_2$	$2.1_{-0.1}^{+0.1}$	$2.1_{-0.1}^{+0.1}$	$2.2_{-0.1}^{+0.1}$	$2.3_{-0.0}^{+0.0}$	$2.0_{-0.1}^{+0.1}$
$a_3$	$2.2_{-0.1}^{+0.1}$	$2.2_{-0.1}^{+0.1}$	$2.4_{-0.1}^{+0.1}$	$2.5_{-0.1}^{+0.1}$	$2.1_{-0.1}^{+0.1}$
$BH_{\text{ret}} [\%]$	$9.2_{-3.7}^{+5.5}$	$9.2_{-3.7}^{+5.6}$	$13_{-5.0}^{+8.7}$	$8.1_{-4.1}^{+14}$	$1.8_{-1.2}^{+1.9}$
$d [\text{kpc}]$	$9.51_{-0.04}^{+0.06}$	$9.51_{-0.04}^{+0.06}$	$8.72_{-0.01}^{+0.01}$	$8.727_{-0.002}^{+0.001}$	$8.824_{-0.002}^{+0.002}$
Good Fit?	✓	✗	✓	✗	✓

Table 3.5: Best-fitting parameters with  $1\sigma$  uncertainties for (10.1–10.5).

Parameter	10.6	10.7	10.8	10.9	10.10
$W_0$	$2.05_{-0.03}^{+0.05}$	$3.00_{-0.11}^{+0.13}$	$2.54_{-0.22}^{+0.20}$	$2.98_{-0.12}^{+0.13}$	$2.88_{-0.14}^{+0.13}$
$M$	$0.61_{-0.00}^{+0.00}$	$0.33_{-0.00}^{+0.00}$	$0.44_{-0.01}^{+0.01}$	$0.33_{-0.00}^{+0.01}$	$0.40_{-0.01}^{+0.01}$
$r_h$	$4.56_{-0.04}^{+0.04}$	$4.61_{-0.04}^{+0.04}$	$4.75_{-0.05}^{+0.06}$	$4.58_{-0.05}^{+0.05}$	$4.77_{-0.05}^{+0.04}$
$r_a$	$0.14_{-0.02}^{+0.07}$	$0.41_{-0.07}^{+0.08}$	$0.48_{-0.08}^{+0.10}$	$0.41_{-0.07}^{+0.07}$	$0.57_{-0.09}^{+0.10}$
$\gamma$	$1.02_{-0.07}^{+0.06}$	$0.53_{-0.12}^{+0.13}$	$1.77_{-0.19}^{+0.20}$	$0.63_{-0.12}^{+0.13}$	$1.27_{-0.17}^{+0.19}$
$\delta$	$0.31_{-0.01}^{+0.01}$	$0.42_{-0.03}^{+0.02}$	$0.34_{-0.03}^{+0.03}$	$0.42_{-0.03}^{+0.03}$	$0.37_{-0.03}^{+0.02}$
$s_2$	$14_{-1.1}^{+0.9}$	$5.9_{-3.4}^{+4.5}$	$9.2_{-3.6}^{+3.6}$	$7.4_{-4.0}^{+4.5}$	$8.5_{-3.6}^{+3.8}$
$F$	$7.30_{-0.14}^{+0.14}$	$4.02_{-0.59}^{+0.73}$	$6.13_{-0.77}^{+0.78}$	$3.97_{-0.56}^{+0.68}$	$4.67_{-0.71}^{+0.88}$
$a_1$	$2.04_{-0.05}^{+0.05}$	$0.98_{-0.05}^{+0.05}$	$1.48_{-0.05}^{+0.05}$	$1.01_{-0.05}^{+0.05}$	$1.29_{-0.06}^{+0.06}$
$a_2$	$2.05_{-0.06}^{+0.11}$	$2.32_{-0.04}^{+0.02}$	$2.17_{-0.10}^{+0.09}$	$2.32_{-0.03}^{+0.02}$	$2.26_{-0.07}^{+0.06}$
$a_3$	$2.07_{-0.06}^{+0.13}$	$3.20_{-0.10}^{+0.13}$	$2.26_{-0.12}^{+0.11}$	$3.09_{-0.18}^{+0.12}$	$2.40_{-0.09}^{+0.13}$
$BH_{\text{ret}}$	$6.3_{-1.8}^{+5.1}$	$37_{-15}^{+9}$	$13_{-6.3}^{+8.9}$	$28_{-15}^{+14}$	$11_{-4.2}^{+8.3}$
$d [\text{kpc}]$	$9.325_{-0.006}^{+0.007}$	$7.907_{-0.001}^{+0.002}$	$9.446_{-0.064}^{+0.078}$	$7.981_{-0.000}^{+0.001}$	$8.996_{-0.102}^{+0.106}$
Good Fit?	✗	✓	✓	✗	✓

Table 3.6: Best-fitting parameters with  $1\sigma$  uncertainties for models 10.6–10.10.

Parameter	25.1	25.2	25.3	25.4	25.5
$W_0$	$2.67^{+0.16}_{-0.19}$	$2.16^{+0.08}_{-0.08}$	$2.03^{+0.03}_{-0.02}$	$2.07^{+0.02}_{-0.03}$	$2.01^{+0.00}_{-0.00}$
$M$	$0.52^{+0.00}_{-0.00}$	$0.56^{+0.00}_{-0.00}$	$0.77^{+0.00}_{-0.00}$	$0.64^{+0.00}_{-0.00}$	$1.08^{+0.00}_{-0.00}$
$r_h$	$4.75^{+0.04}_{-0.04}$	$4.21^{+0.03}_{-0.03}$	$4.55^{+0.03}_{-0.03}$	$4.66^{+0.02}_{-0.01}$	$4.75^{+0.00}_{-0.00}$
$r_a$	$0.32^{+0.10}_{-0.05}$	$0.11^{+0.03}_{-0.02}$	$0.02^{+0.02}_{-0.01}$	$0.39^{+0.02}_{-0.02}$	$0.37^{+0.00}_{-0.00}$
$\gamma$	$0.77^{+0.12}_{-0.11}$	$0.79^{+0.08}_{-0.07}$	$0.45^{+0.05}_{-0.05}$	$0.56^{+0.02}_{-0.03}$	$0.34^{+0.00}_{-0.00}$
$\delta$	$0.34^{+0.04}_{-0.03}$	$0.31^{+0.01}_{-0.01}$	$0.30^{+0.00}_{-0.00}$	$0.36^{+0.00}_{-0.00}$	$0.37^{+0.00}_{-0.00}$
$s_2$	$13^{+1.4}_{-2.5}$	$14^{+1.0}_{-1.4}$	$14^{+0.4}_{-0.7}$	$15^{+0.3}_{-0.7}$	$8.6^{+0.0}_{-0.0}$
$F$	$7.2^{+0.2}_{-0.5}$	$7.3^{+0.2}_{-0.2}$	$7.5^{+0.0}_{-0.0}$	$7.4^{+0.0}_{-0.1}$	$7.3^{+0.0}_{-0.0}$
$a_1$	$1.77^{+0.04}_{-0.04}$	$1.97^{+0.05}_{-0.05}$	$2.34^{+0.01}_{-0.01}$	$2.33^{+0.01}_{-0.01}$	$2.35^{+0.00}_{-0.00}$
$a_2$	$1.85^{+0.06}_{-0.06}$	$2.02^{+0.06}_{-0.06}$	$2.35^{+0.01}_{-0.01}$	$2.35^{+0.00}_{-0.00}$	$2.35^{+0.00}_{-0.00}$
$a_3$	$1.94^{+0.07}_{-0.06}$	$2.10^{+0.06}_{-0.06}$	$2.36^{+0.02}_{-0.01}$	$2.44^{+0.02}_{-0.02}$	$2.37^{+0.00}_{-0.00}$
$BH_{\text{ret}}$	$1.6^{+1.0}_{-0.9}$	$4.5^{+2.3}_{-1.7}$	$3.7^{+1.6}_{-1.6}$	$24^{+3.1}_{-1.3}$	$15.5^{+0.1}_{-0.0}$
$d[\text{kpc}]$	$9.22^{+0.01}_{-0.00}$	$8.53^{+0.00}_{-0.00}$	$8.81^{+0.00}_{-0.00}$	$8.79^{+0.00}_{-0.00}$	$8.80^{+0.00}_{-0.00}$
Good Fit?	✓	✓	✗	✓	✓

Table 3.7: Best-fitting parameters with  $1\sigma$  uncertainties for (25.1-25.5).

Parameter	25.6	25.7	25.8	25.9	25.10
$W_0$	$2.25^{+0.19}_{-0.16}$	$2.13^{+0.12}_{-0.09}$	$2.03^{+0.03}_{-0.02}$	$2.07^{+0.08}_{-0.05}$	$2.07^{+0.08}_{-0.05}$
$M$	$0.52^{+0.01}_{-0.01}$	$0.58^{+0.00}_{-0.00}$	$0.69^{+0.00}_{-0.00}$	$0.74^{+0.01}_{-0.01}$	$0.74^{+0.01}_{-0.01}$
$r_h$	$4.89^{+0.06}_{-0.05}$	$5.09^{+0.04}_{-0.05}$	$4.76^{+0.03}_{-0.03}$	$4.89^{+0.08}_{-0.05}$	$4.89^{+0.08}_{-0.05}$
$r_a$	$0.37^{+0.07}_{-0.06}$	$0.42^{+0.08}_{-0.07}$	$0.03^{+0.02}_{-0.01}$	$2.9^{+1.2}_{-0.3}$	$2.9^{+1.2}_{-0.3}$
$\gamma$	$1.9^{+0.1}_{-0.2}$	$1.9^{+0.1}_{-0.1}$	$0.38^{+0.05}_{-0.04}$	$2.1^{+0.1}_{-0.1}$	$2.1^{+0.1}_{-0.1}$
$\delta$	$0.32^{+0.02}_{-0.01}$	$0.32^{+0.02}_{-0.02}$	$0.30^{+0.00}_{-0.00}$	$0.34^{+0.01}_{-0.01}$	$0.34^{+0.01}_{-0.01}$
$s_2$	$10^{+3.2}_{-3.5}$	$11^{+2.4}_{-3.1}$	$14.6^{+0.3}_{-0.5}$	$14.6^{+0.4}_{-0.5}$	$14.6^{+0.4}_{-0.5}$
$F$	$7.2^{+0.2}_{-0.4}$	$7.3^{+0.1}_{-0.2}$	$7.5^{+0.0}_{-0.0}$	$7.5^{+0.1}_{-0.1}$	$7.5^{+0.1}_{-0.1}$
$a_1$	$2.35^{+0.04}_{-0.04}$	$2.35^{+0.03}_{-0.03}$	$2.33^{+0.01}_{-0.01}$	$2.33^{+0.01}_{-0.01}$	$2.33^{+0.01}_{-0.01}$
$a_2$	$2.35^{+0.02}_{-0.02}$	$2.35^{+0.01}_{-0.01}$	$2.35^{+0.01}_{-0.01}$	$2.35^{+0.01}_{-0.01}$	$2.35^{+0.01}_{-0.01}$
$a_3$	$2.34^{+0.02}_{-0.01}$	$2.34^{+0.02}_{-0.01}$	$2.34^{+0.02}_{-0.01}$	$2.34^{+0.02}_{-0.01}$	$2.34^{+0.02}_{-0.01}$
$BH_{\text{ret}}$	$6.5^{+1.8}_{-2.4}$	$8.5^{+2.2}_{-3.3}$	$9.3^{+0.7}_{-1.4}$	$6.7^{+0.9}_{-1.3}$	$6.7^{+0.9}_{-1.3}$
$d[\text{kpc}]$	$8.99^{+0.01}_{-0.01}$	$8.94^{+0.01}_{-0.00}$	$8.81^{+0.00}_{-0.00}$	$8.90^{+0.00}_{-0.00}$	$8.90^{+0.00}_{-0.00}$
Good Fit?	✗	✗	✗	✗	✓

Table 3.8: Best-fitting parameters with  $1\sigma$  uncertainties for (25.6-25.10).

# Chapter 4

## Inferred black hole populations for different mock pulsar datasets

In this chapter, we compare the resulting inferred BH population from the model fits of the previous chapter to the true BH populations. The true BH population is from the CMC snapshot from which the mock pulsars were sampled. In our snapshot, the true number of BHs is 258, the BH mass fraction of the cluster is 0.87% and the total mass in BHs is  $3665.51 \text{ M}_\odot$ . The inferred mass fractions in BHs with  $1\sigma$  uncertainty from all good fits are shown in Table 4.1 and the bad fits are not included discussed in Chapter 3.

While some of the fits satisfactorily recover the mass fraction of BHs in the cluster, there are a number of fits where true BH mass fractions are not recovered even with uncertainties of factors of 3. Cases where the BH mass fraction is not well recovered seem to be linked to the problems discussed in the previous chapter, which occur when many pulsars have large positive spin  $\dot{P}/P$  due to intrinsic spin-down. In Figure 4.1, we show the posterior probability distribution of the BH mass fraction for two different cases. The posterior probability distribution for CMC6402-25PULSARS4 is in much better agreement with the true value than CMC6402-25PULSARS6. This may be explained with Figure 4.2, where we can see that fewer pulsars have large positive spin-period derivatives in the case of CMC6402-25PULSARS4.

Mock dataset	$f_{\text{BH}}$	$M_{\text{BH}} [M_{\odot}]$
CMC6402-5PULSARS1	$0.64^{+0.17\%}_{-0.15\%}$	$2462.7^{+665}_{-600}$
CMC6402-5PULSARS2	$0.92^{+0.21\%}_{-0.20\%}$	$3721.9^{+838}_{-801}$
CMC6402-5PULSARS3	$1.81^{+0.25\%}_{-0.25\%}$	$10517.1^{+1476}_{-1451}$
CMC6402-5PULSARS4	$1.01^{+0.34\%}_{-0.25\%}$	$4332.4^{+1439}_{-1039}$
CMC6402-5PULSARS6	$0.79^{+0.21\%}_{-0.14\%}$	$3115.0^{+864}_{-596}$
CMC6402-5PULSARS7	$1.62^{+0.34\%}_{-0.34\%}$	$7351.0^{+1499}_{-1463}$
CMC6402-5PULSARS8	$1.99^{+0.51\%}_{-0.41\%}$	$9898.8^{+2456}_{-1949}$
CMC6402-10PULSARS1	$1.24^{+0.25\%}_{-0.25\%}$	$5416.1^{+1094}_{-1104}$
CMC6402-10PULSARS3	$0.97^{+0.16\%}_{-0.17\%}$	$3892.1^{+614}_{-672}$
CMC6402-10PULSARS5	$0.34^{+0.27\%}_{-0.21\%}$	$1801.3^{+1415}_{-1139}$
CMC6402-10PULSARS7	$0.17^{+0.05\%}_{-0.07\%}$	$562.8^{+177}_{-245}$
CMC6402-10PULSARS8	$1.48^{+0.26\%}_{-0.31\%}$	$6412.4^{+1086}_{-1273}$
CMC6402-10PULSARS10	$0.81^{+0.19\%}_{-0.16\%}$	$3231.1^{+794}_{-664}$
CMC6402-25PULSARS1	$0.61^{+0.25\%}_{-0.32\%}$	$3175.7^{+1647}_{-1276}$
CMC6402-25PULSARS2	$0.82^{+0.18\%}_{-0.18\%}$	$4551.5^{+1001}_{-982}$
CMC6402-25PULSARS4	$0.90^{+0.04\%}_{-0.04\%}$	$5779.6^{+265}_{-235}$
CMC6402-25PULSARS5	$0.76^{+0.01\%}_{-0.01\%}$	$8238.8^{+133}_{-103}$
CMC6402-25PULSARS10	$0.76^{+0.17\%}_{-0.14\%}$	$2976.1^{+684}_{-600}$
CMC6402-NoPULSARS	$0.64^{+0.22\%}_{-0.17\%}$	$2471.7^{+870}_{-683}$

Table 4.1: Mock datasets with inferred black hole mass fraction  $f_{\text{BH}}$  and total BH mass  $M_{\text{BH}}$  with  $1\sigma$  uncertainties.

The width of the posterior probability distribution (and therefore the uncertainty in the inferred mass fraction in BHs) also varies between the fits to mock data containing different numbers of pulsars. Figure 4.3 shows the posterior probability distribution for the mass fraction in BHs for a mock dataset with 5 pulsars (CMC6402-5PULSARS4), 25 pulsars (CMC6402-25PULSARS4) and no pulsars (CMC6402-NoPULSARS) with their comparison with the true value from the snapshot. We observe that including more pulsars gives a significantly narrower posterior distribution for the mass fraction of BHs. All of these 3 fits are in excellent agreement

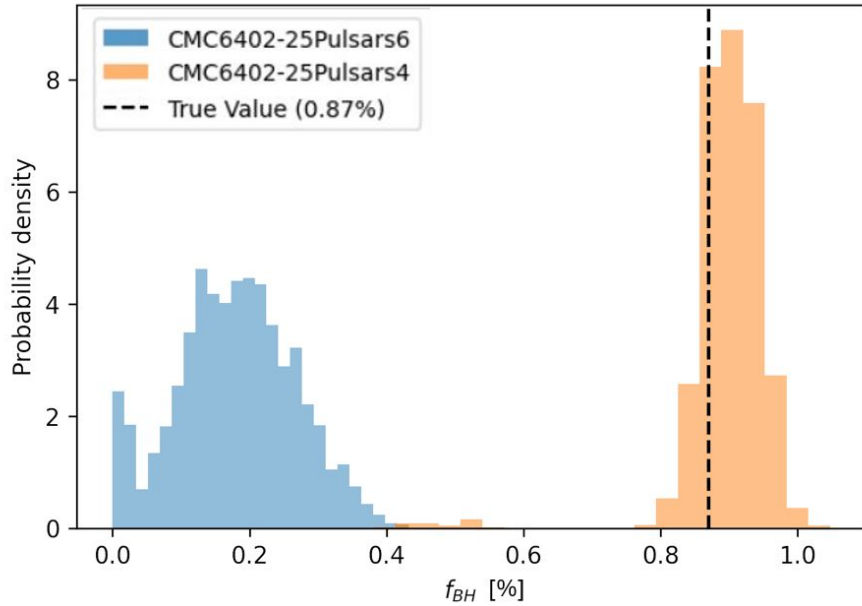


Figure 4.1: Posterior probability distribution of the amount of BHs in CMC6402-25PULSARS6 fit in blue and CMC6402-25PULSARS4 fit in orange.

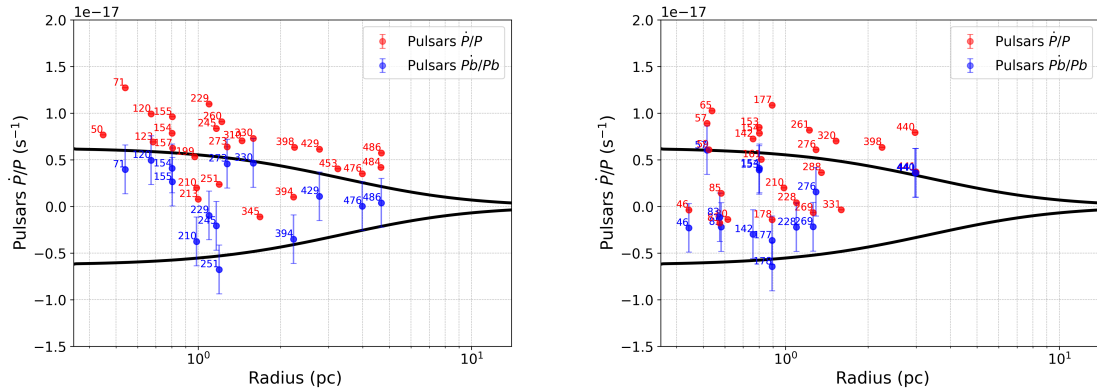


Figure 4.2: Minimum and maximum values of allowed  $\frac{\dot{P}}{P}$  due to the cluster potential for CMC6402-25PULSARS6 at left and CMC6402-25PULSARS4 at right. The black lines here are calculated from the underlying mass distribution in the snapshot. The dots are all the mock pulsars plotted with all components of spin  $\frac{\dot{P}}{P}$  in red and  $\frac{\dot{P}_b}{P_b}$  in blue.

with the observations, but the width of the posterior distribution shows that when fitting models to datasets with fewer pulsars the BH mass fraction is inferred with less precision. However, for both mock datasets that include pulsars, the posterior

distributions have their peak almost exactly at the true value. However, the mock dataset containing no pulsars has a posterior probability distribution for the mass fraction in BHs that peaks at a lower value than the true value and is also broader than the distributions for datasets including pulsars.

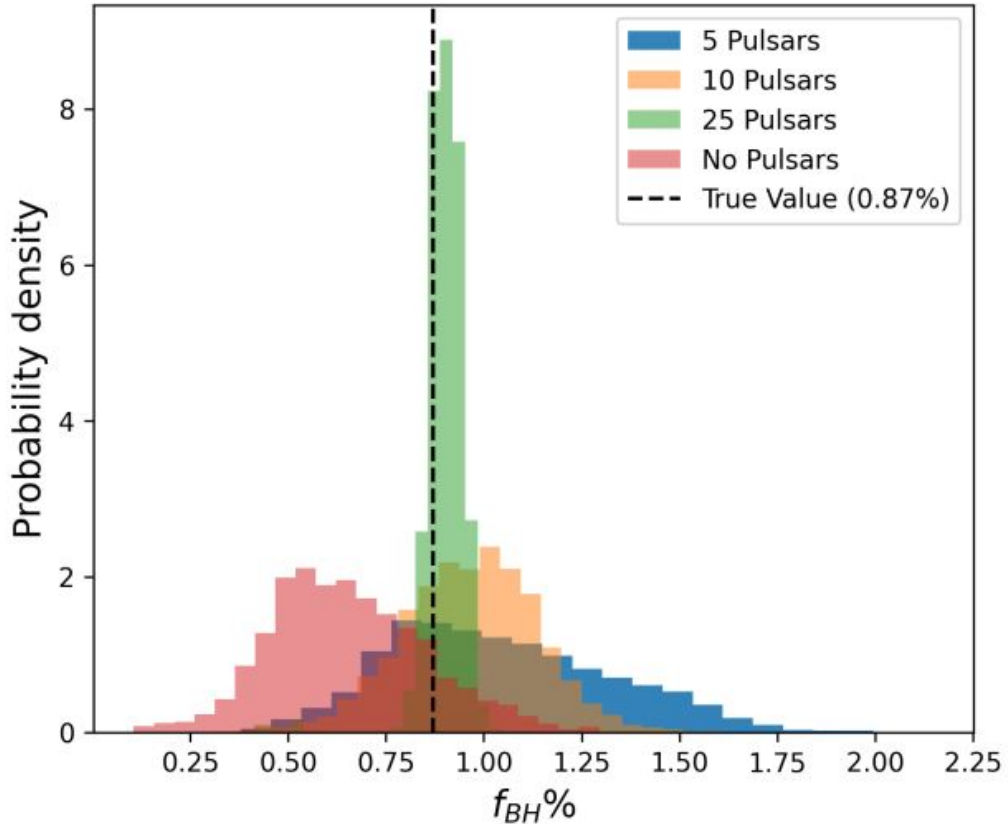


Figure 4.3: Posterior probability distribution for the mass fractions of BHs in CMC6402-5PULSARS4, CMC6402-25PULSARS4 fits and CMC6402-NOPULSARS. The true value of  $f_{BH}$  is shown by the black dashed vertical line.

In Figure 4.4, we compare the inferred BH mass fractions ( $f_{BH}$ ) from different fits to mock datasets containing various sets of pulsars, against the true BH mass fraction value ( $f_{BH,\text{true}}$ ) from the CMC model snapshot. The “good fits” are those that match well with the observations and are displayed in the plot. In contrast, the

“bad fits”, which do not fully agree with the observational data, are excluded from the plot. These bad fits correspond to mock pulsar datasets 5.5, 5.9, 10.2, 10.4, 10.6, 10.9, 25.3, 25.6, 25.7, 25.8 and 25.9.

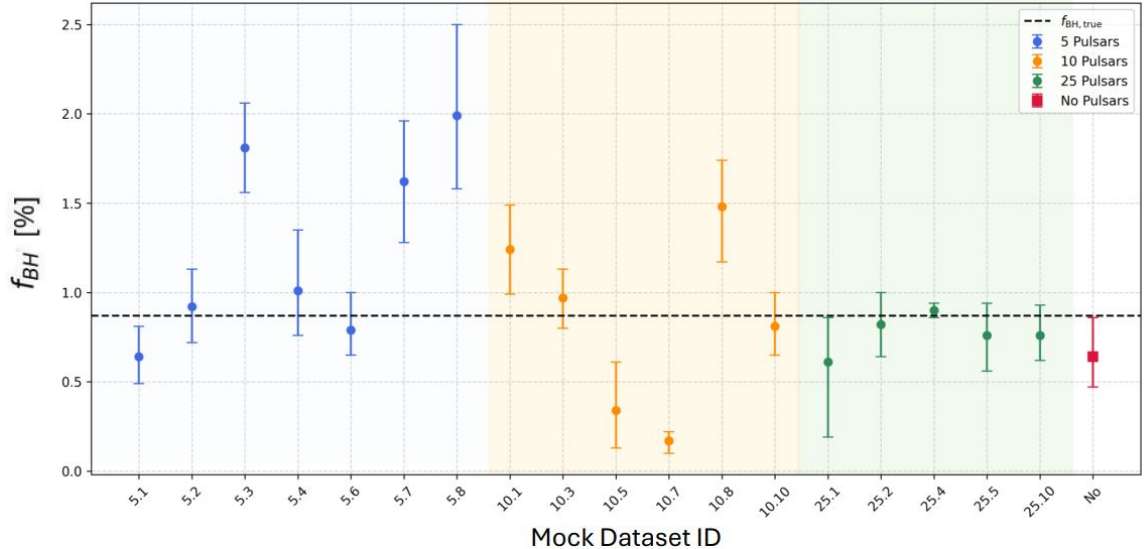


Figure 4.4: The  $f_{\text{BH}}$  values inferred based on the mock observations with different sets of pulsars (good fits only) as labeled on the x axis. The true value  $f_{\text{BH},\text{true}}$  is shown as a horizontal dashed line. The error bars are showing  $1\sigma$  uncertainties.

This comparison of inferred BH mass fractions across different mock observations with different numbers of pulsars, demonstrates the accuracy and precision of the recovered mass fraction in BHs in Figure 4.4. The mock datasets include different realizations with 5, 10, and 25 pulsars each with spin period derivatives and among them 3, 5 and 12 pulsars have orbital period derivatives respectively (Table 3.2). The results show that good fits to mock datasets with 5 and 10 pulsars exhibit minor but significant deviations from the true value, considering their associated uncertainties on  $f_{\text{BH}}$ . In contrast, the results for the mock dataset with 25 pulsars agree more closely with the true value, demonstrating improved precision in the inferred mass fraction in

BHs compared to datasets with fewer pulsars. The plot highlights that including more pulsars improves the estimation of the BH mass fraction. By performing additional model fits on varied realizations of mock pulsar samples, we could further verify the trend observed in Figure 4.4. This would help better quantify the true uncertainties (including systematic effects) in the inferred BH mass fraction when applying our method.

Additionally, the fit to the mock dataset without pulsar data, consistent with observations, yields  $f_{\text{BH}} = 0.64^{+0.22\%}_{-0.17\%}$ , also close to the true value. Overall, the BH mass fraction is recovered well when fitting multimass models to GC observations (as shown in [Dickson et al. 2024](#)). While we confirm this result, we further demonstrate that the inferred BH mass fraction is better constrained as the number of pulsars with timing data increases.

# Chapter 5

## Mass models of the globular cluster M62

### 5.1 INTRODUCTION TO M62

M62 is a massive and luminous globular cluster (GC) located in the dense region of the Galactic bulge of the Milky Way and exhibiting one of the highest stellar encounter rates known (e.g. [Oh et al., 2020](#)). With an extremely dense core containing approximately 150,000 stars and being one of the closest globular clusters to the Galactic center, M62 serves as an ideal laboratory for studying dynamical processes, as we have information about its physical properties including location, mass, radius, and 3D velocity.

The key motivation for studying M62 lies in its population of 10 known millisecond pulsars (MSPs) with precise timing solutions, which provide powerful probes for investigating dynamical interactions in the cluster core and its central mass distribution. The cluster's debated core-collapsed status - resulting from gravitational contraction that may have ejected all the black holes from the core, makes it particularly intriguing. By exploring potential dark remnants in its center, we can better understand how black holes are retained and evolve in such dense environments and address the fundamental question of whether M62 is truly core-collapsed as suggested

by Djorgovski and Meylan (1993).

Name of the fit	Pulsars	Distance (kpc) prior
M62Gaussian-WithPulsar	✓	Gaussian [6.41, 0.1]
M62Gaussian-NoPulsars		Gaussian [6.41, 0.1]
M62Uniform-WithPulsars	✓	Uniform prior [5,7]
M62Uniform-NoPulsars		Uniform prior [5,7]
M62-OnlyPulsars	✓	Gaussian [6.41, 0.1]

Table 5.1: Different model fits with pulsars and distance priors. We use a Gaussian prior with the distance measurement and its uncertainty providing the mean  $\mu$  and standard deviation  $\sigma$  of the prior. Uniform priors defines a range of allowed values providing the minimum and the maximum values of the range.

As we mentioned before, M62 hosts 10 known binary MSPs, including one eclipsing redback (a pulsar with a massive, non-degenerate companion Vleeschower et al., 2024). In this study, we exclude the redback system, assuming none of the pulsars are actively accreting, and focus on the remaining 9 pulsars. Among these, 8 pulsars have complete timing solutions for their spin periods and period derivatives, while 5 also have measured orbital periods and period derivatives (Vleeschower et al., 2024). We incorporate these timing solutions for both spin and orbital periods and period derivatives for all 8 pulsars in our analysis, as detailed in Table A.1 and A.2.

In this chapter, we show the results of fitting multimass dynamical models to observations of M62 (including pulsar timing data) to constrain the mass distribution and BH population of this cluster. We explore different priors for the heliocentric distance ( $d$  in kpc): (1) a Gaussian distribution around 6.41 kpc with 0.1 kpc standard deviation and (2) a uniform prior, ranging from 5 to 7 kpc, taken to restrict the distance to a range of reasonable values.  $d = 6.412 \pm 0.105$  kpc is the mean helio-

centric distance for M62 from a compilation of measurements from different studies (Baumgardt and Vasiliev, 2021). We fit the models to observations of velocity dispersion profiles, number density profile and local stellar mass function (Dickson et al., 2023), with and without pulsar timing data for these two different priors shown in Table 5.1. We also perform a fit using pulsar data but excluding the LOS velocity dispersion and proper motion dispersion profiles: M62-ONLYPULSARS.

## 5.2 MODEL FITS AND COMPARISON

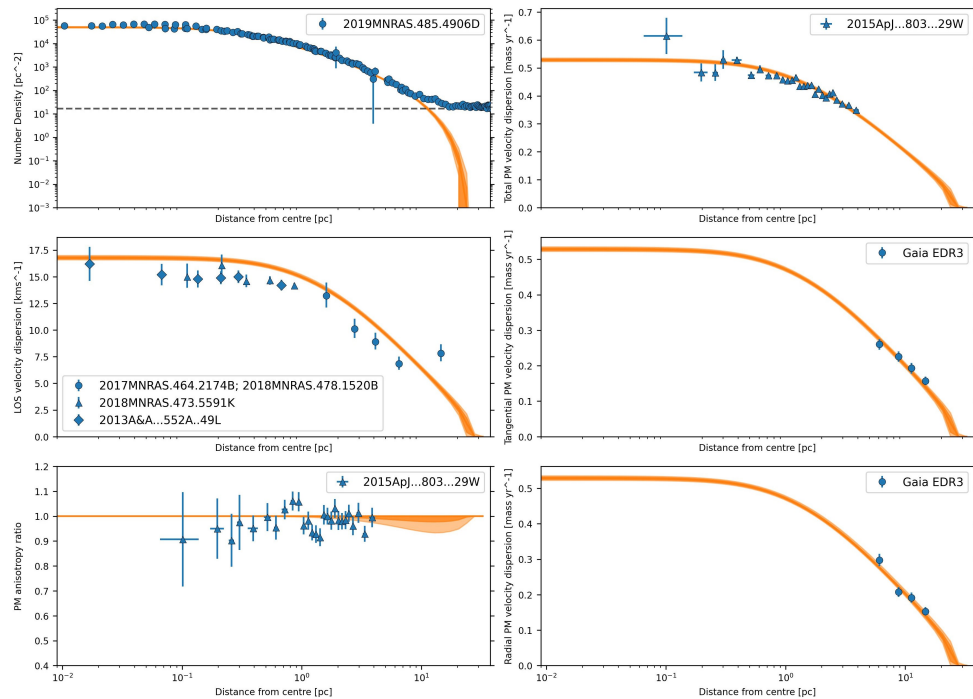


Figure 5.1: Best-fitting model (in orange) for the M62UNIFORM-NoPULSARS fit and different datasets (in blue). Top left: Model fit to the projected number density profile. Middle left: Model fit to the line-of-sight velocity dispersion profile. Bottom left: Model of the proper motion anisotropy profile. Right panels: Model of the total proper motion dispersion profile, separated into tangential (middle-right panel) and radial (bottom-right panel) components. The legend of the different blue dots represents different observational sources.

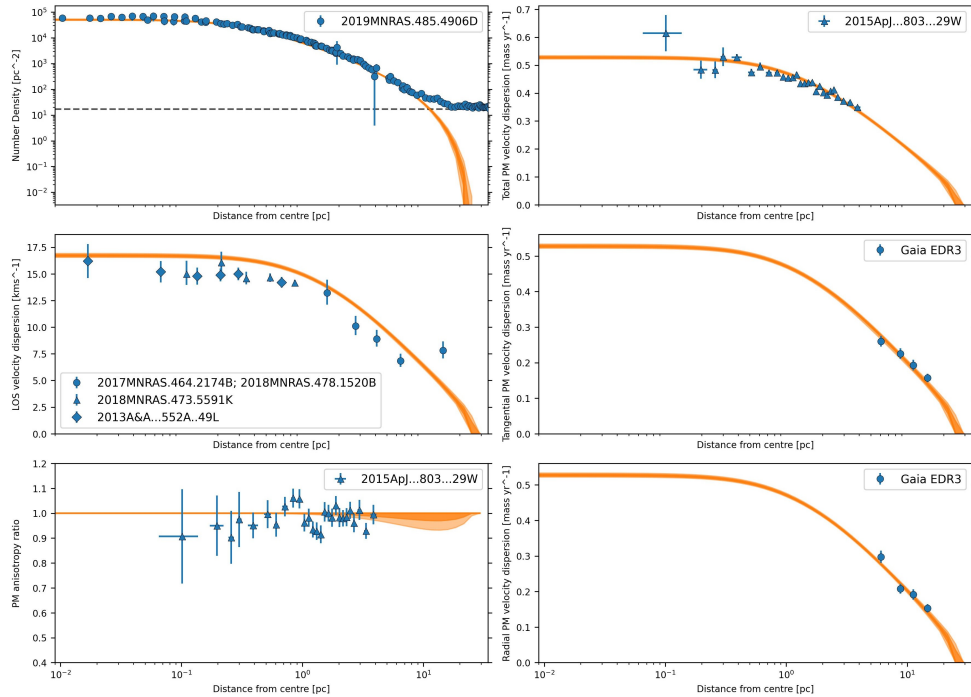


Figure 5.2: Best-fitting model (in orange) for the M62UNIFORM-WITHPULSARS fit and different datasets (in blue).

In Figure 5.1 and Figure 5.2, the fits of M62UNIFORM-NOPULSARS and M62UNIFORM-WITHPULSARS reveal that the best-fitting models are similar to each other and generally agree well with the observations, except for the LOS velocity dispersion profile, which is slightly overestimated in the models. From Table 5.2 we see these fits favour a larger distance. We run similar fits for M62GAUSSIAN-WITHPULSAR, M62GAUSSIAN-NoPULSARS where the Gaussian prior strongly favours best-fitting models with a distance around 6.4 kpc. These models are in better agreement with the LOS velocity dispersion profile (Figure 5.3) and the best-fitting model parameters are presented in Table 5.2. Consequently, we plot the minimum and maximum allowed values of  $\frac{\dot{P}}{P}$  due to the cluster potential with the measured pulsar spin and orbital period derivatives. It is clearly shown in Figure 5.4 that the best-fitting

models for M62UNIFORM-WITHPULSARS (and M62UNIFORM-NOPULSARS) prefer a higher mass in the centre to accommodate all observed pulsars compared to the fits M62GAUSSIAN-WITHPULSARS (and M62GAUSSIAN-NOPULSARS). One way to increase the mass of the model for a given angular size of the cluster is to place the cluster at a larger distance. As a result, the LOS velocity dispersion profile for this heliocentric distance prior is slightly larger than the observations.

Parameters	Dataset and priors combinations				
	Uniform-NoP	Uniform-WithP	Gaussian-NoP	Gaussian-WithP	Only P
$W_0$	$6.179^{+0.11}_{-0.11}$	$6.229^{+0.12}_{-0.12}$	$6.33^{+0.14}_{-0.14}$	$5.939^{+0.23}_{-0.23}$	$5.233^{+0.3}_{-0.3}$
$M[10^6 M_\odot]$	$0.76^{+0.02}_{-0.02}$	$0.759^{+0.01}_{-0.01}$	$0.72^{+0.05}_{-0.05}$	$0.71^{+0.03}_{-0.03}$	$0.921^{+0.05}_{-0.05}$
$r_h[\text{pc}]$	$2.892^{+0.06}_{-0.06}$	$2.907^{+0.05}_{-0.05}$	$3.02^{+0.14}_{-0.14}$	$3.079^{+0.11}_{-0.11}$	$3.021^{+0.12}_{-0.12}$
$r_a$	$2.948^{+1.37}_{-1.37}$	$3.036^{+1.30}_{-1.30}$	$1.81^{+1.47}_{-1.47}$	$2.054^{+1.33}_{-1.33}$	$1.523^{+1.41}_{-1.41}$
$g$	$1.229^{+0.05}_{-0.05}$	$1.211^{+0.05}_{-0.05}$	$1.035^{+0.06}_{-0.06}$	$1.041^{+0.06}_{-0.06}$	$0.82^{+0.13}_{-0.13}$
$\delta$	$0.496^{+0.004}_{-0.004}$	$0.496^{+0.004}_{-0.004}$	$0.495^{+0.01}_{-0.01}$	$0.495^{+0.01}_{-0.01}$	$0.477^{+0.02}_{-0.02}$
$s_2$	$0.20^{+0.06}_{-0.06}$	$0.20^{+0.04}_{-0.04}$	$0.26^{+0.07}_{-0.07}$	$0.237^{+0.06}_{-0.06}$	$0.22^{+0.03}_{-0.03}$
$F$	$3.214^{+0.37}_{-0.37}$	$3.093^{+0.36}_{-0.36}$	$2.86^{+0.36}_{-0.36}$	$2.946^{+0.29}_{-0.29}$	$3.124^{+0.42}_{-0.42}$
$a_1$	$-0.67^{+0.19}_{-0.19}$	$-0.718^{+0.19}_{-0.19}$	$-0.09^{+0.41}_{-0.41}$	$-0.48^{+0.31}_{-0.31}$	$-0.35^{+0.37}_{-0.37}$
$a_2$	$1.372^{+0.1}_{-0.1}$	$1.311^{+0.10}_{-0.10}$	$1.24^{+0.16}_{-0.16}$	$1.321^{+0.08}_{-0.08}$	$1.251^{+0.09}_{-0.09}$
$a_3$	$1.984^{+0.16}_{-0.16}$	$1.975^{+0.23}_{-0.23}$	$2.16^{+0.15}_{-0.15}$	$2.206^{+0.14}_{-0.14}$	$1.9^{+0.17}_{-0.17}$
$\text{BH}_{\text{ret}}[\%]$	$0.215^{+0.06}_{-0.06}$	$0.221^{+0.06}_{-0.06}$	$0.665^{+0.09}_{-0.09}$	$0.666^{+0.09}_{-0.09}$	$0.321^{+0.06}_{-0.06}$
$d[\text{kpc}]$	$6.697^{+0.04}_{-0.04}$	$6.688^{+0.04}_{-0.04}$	$6.481^{+0.05}_{-0.05}$	$6.477^{+0.04}_{-0.04}$	$6.394^{+0.05}_{-0.05}$

Table 5.2: Medians and  $1\sigma$  uncertainties of each model parameter for all five fits of M62 is shown. The naming convention of datasets and priors combination are taken from Table 5.1.

The M62GAUSSIAN-WITHPULSARS and M62GAUSSIAN-NOPULSARS models provide the best compromise between the stellar kinematic data and the heliocentric distance in the fitted profiles. As shown in Figure 5.4, the M62GAUSSIAN-WITHPULSARS model tries to accommodate most of the pulsars. However, due to its prior on the dis-

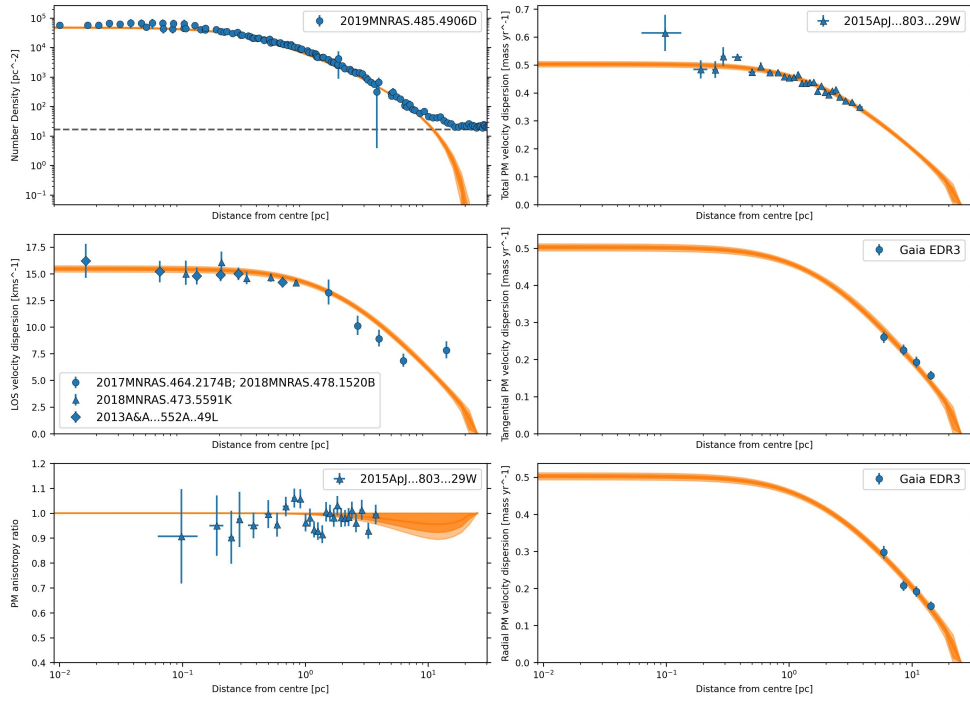


Figure 5.3: Best-fitting model (in orange) for the M62GAUSSIAN-WITHPULSARS fit and different datasets (in blue).

tance, it must strike a balance between matching the observed velocity dispersion profile and favouring a larger central mass concentration. This trade-off prefers a slightly lower mass in the centre of the cluster than the M62UNIFORM-WITHPULSARS model, which prevents it from perfectly containing the period derivatives of all pulsars within the minimum-maximum contours.

Including or not including the pulsars did not make any significant difference to the fits or the parameters in the cases of both distance priors. Figure 5.5 is a corner plot that displays the 2D joint posterior probability distributions for seven key parameters for all the 5 fits mentioned above.

For the fit M62-ONLYPULSARS, that model also preferred more mass in the centre (like M62UNIFORM-WITHPULSARS), as shown in Figure 5.6. It is clear from the plot

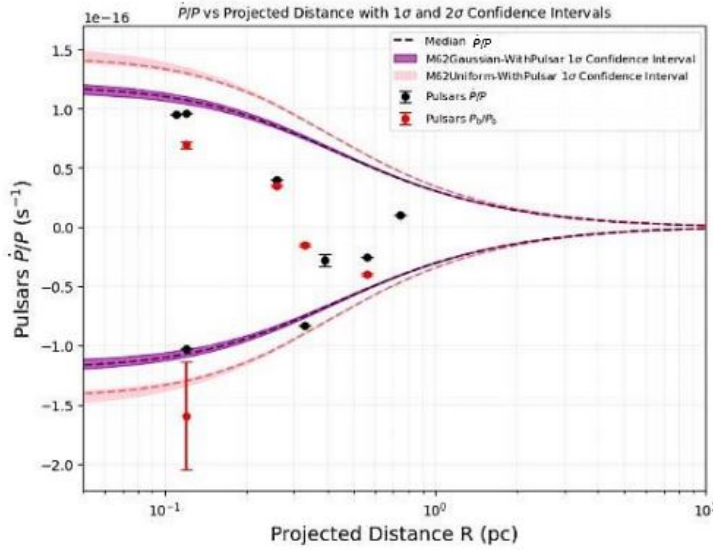


Figure 5.4: Minimum and maximum values of allowed  $\frac{\dot{P}}{P}$  due to the cluster potential for the M62UNIFORM-WITHPULSARS and M62GAUSSIAN-WITHPULSARS models are shown in pink and purple shaded regions respectively with  $1\sigma$  confidence intervals. The observed  $\frac{\dot{P}}{P}$  of the pulsars are shown with black circles and the observed  $\frac{\dot{P}_b}{P_b}$  shown with red circles along with  $1\sigma$  uncertainties

of the minimum and maximum values of  $\frac{\dot{P}}{P}$  allowed from the acceleration in the cluster potential for the best-fitting models. The same inconsistencies with the LOS velocity dispersion and total proper motion velocity dispersion profiles can also be seen in Figure 5.7.

### 5.3 BLACK HOLE POPULATION IN M62

The absence of retained black holes typically indicates a core-collapsed state, as these black holes are what prevents the core of visible stars from collapsing. The best-fitting models for all the cases presented above do not show any obvious evidence for the cluster being core collapsed. The cases with or without including the pul-

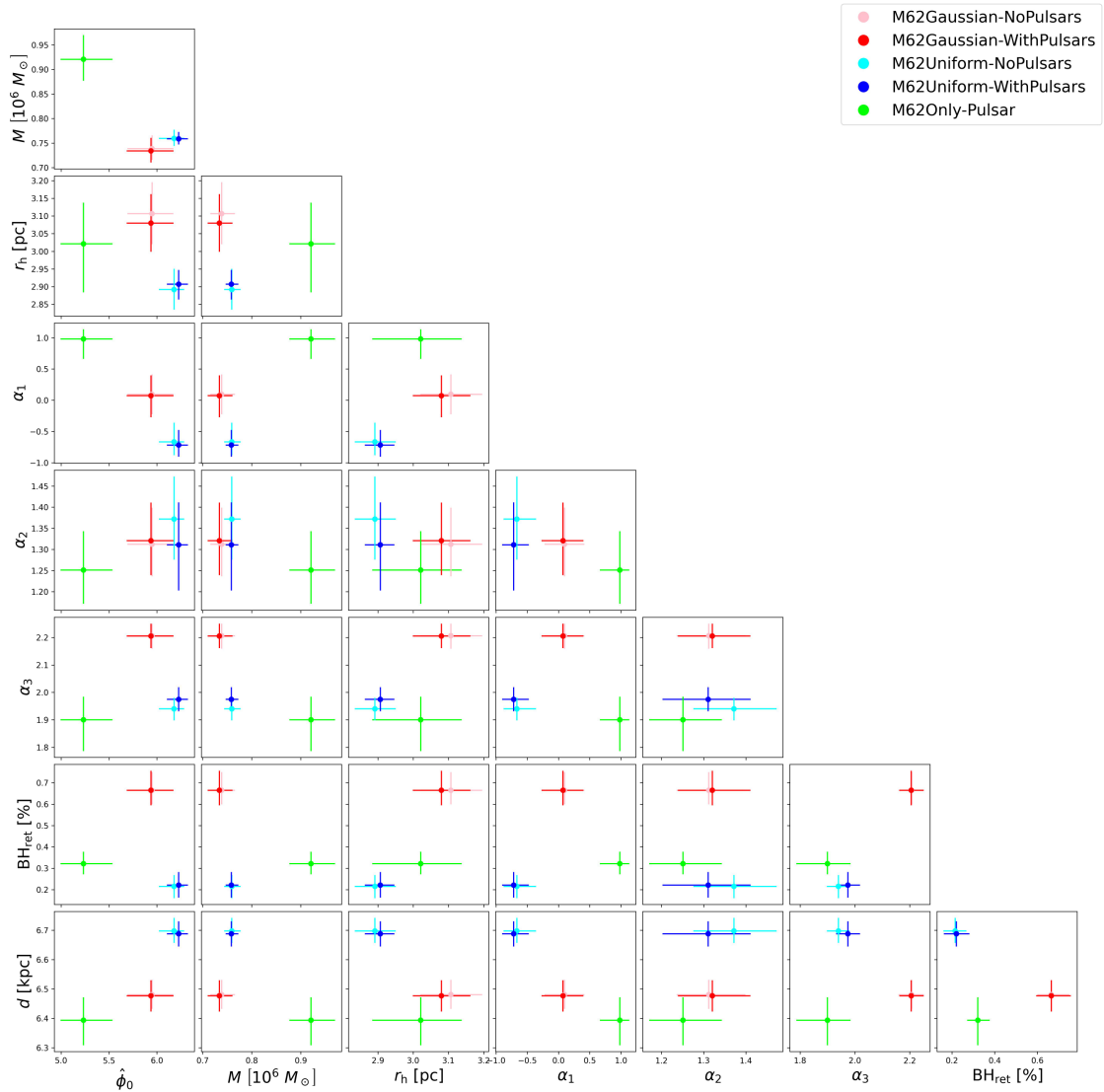


Figure 5.5: 2D joint posterior probability distributions for seven key parameters from different fits of M62.

sar data are very similar in the inferred posterior probability distribution for the cluster mass in BHs (Figure 5.8), and all of the fits prefer some BH mass in the centre as shown in Figure 5.9 and Table 5.2. It is possible that the number of pulsars with measured period derivatives in M62 is still too small to constrain the BH population significantly better than when pulsar data are not considered. That may explain why the M62GAUSSIAN-NOPULSAR and M62UNIFORM-NOPULSAR fits al-

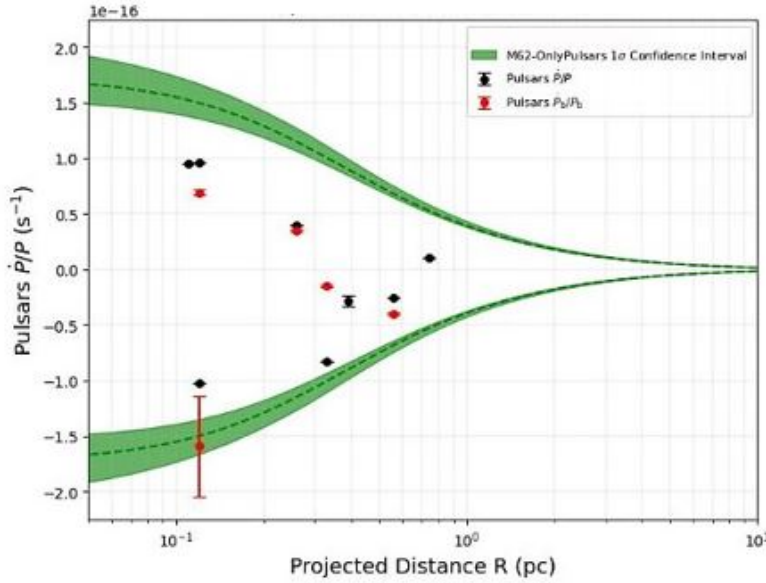


Figure 5.6: Minimum and maximum values of allowed  $\frac{\dot{P}}{P}$  due to the cluster potential for the M62-ONLYPULSARS model is shown in green shaded region with  $1\sigma$  confidence interval. The observed  $\frac{\dot{P}}{P}$  of the pulsars are shown with black circles and the observed  $\dot{P}_b/P_b$  shown with red circles along with  $1\sigma$  uncertainties

ready constrain the mass distribution of M62 very well, since they are fully consistent with the M62GAUSSIAN-WITHPULSARS and M62UNIFORM-WITHPULSAR fits.

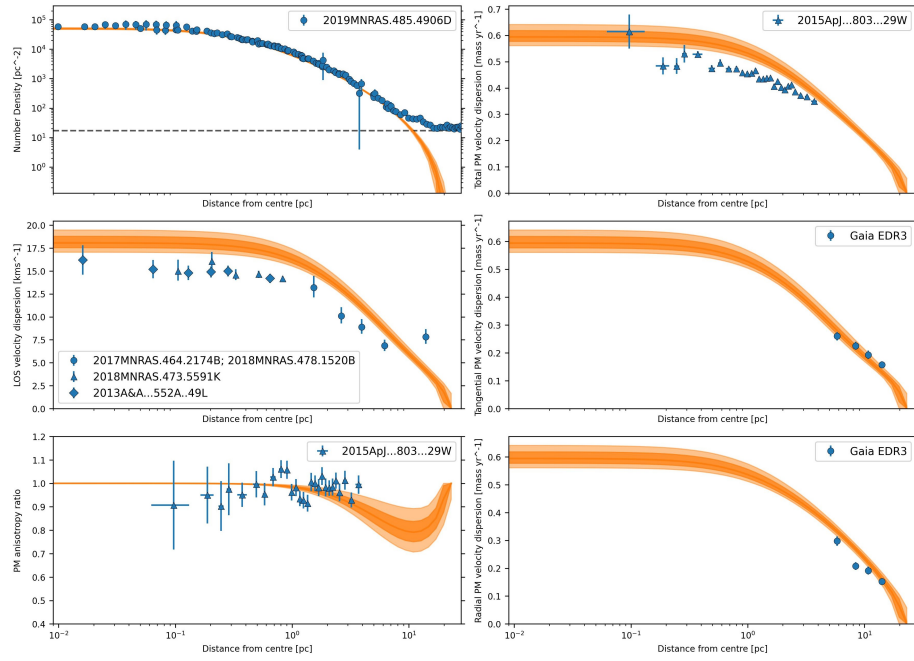


Figure 5.7: Best-fitting model (in orange) for the M62-ONLYPULSARS fit and different datasets (in blue).

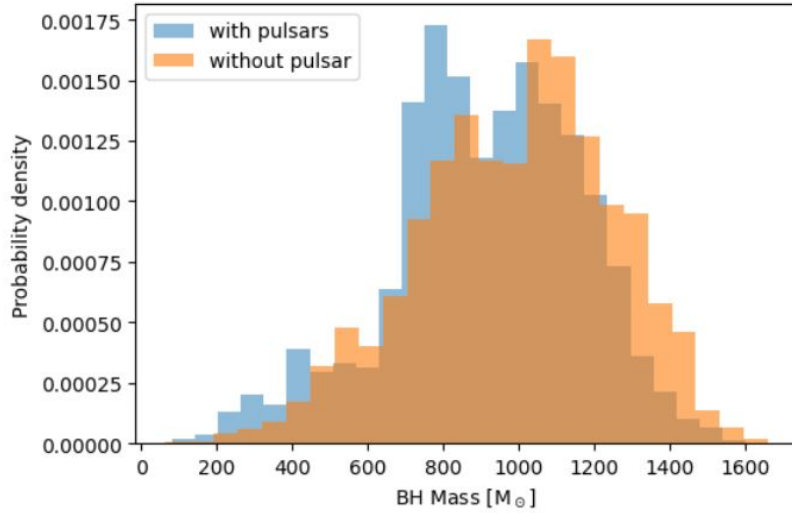
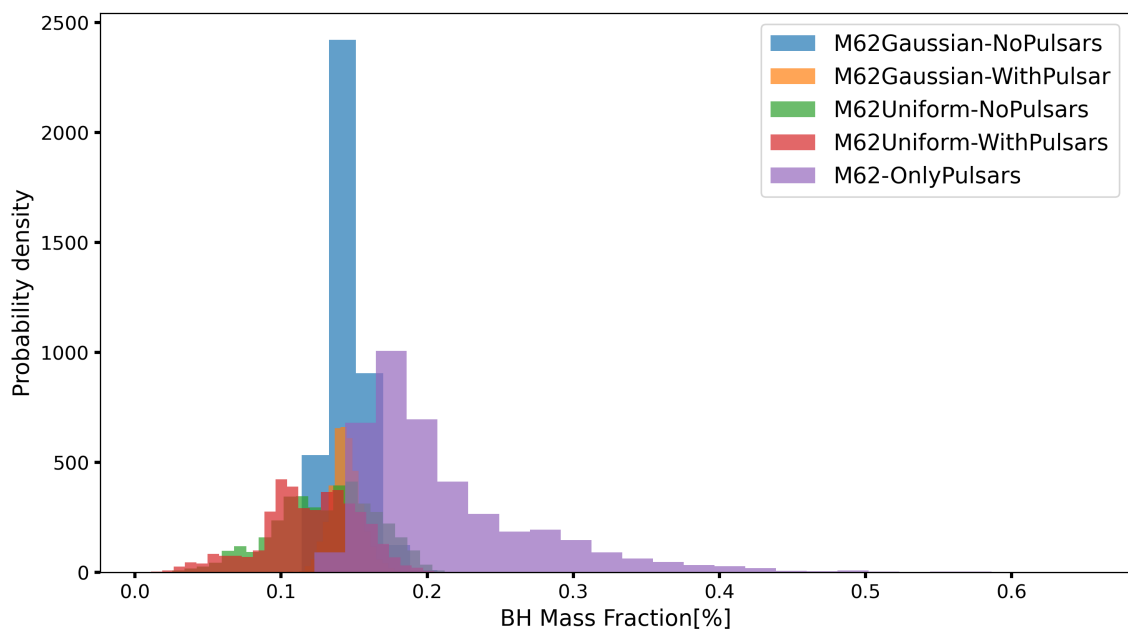


Figure 5.8: Posterior probability distribution of the mass in BHs in M62UNIFORM-WITHPULSARS in blue and M62UNIFORM-NoPULSARS in orange.

Fit	Number of BHs [ $M_{\odot}$ ]
M62Uniform-NoPulsars	149.2 $^{+39}_{-30}$
M62Uniform-WithPulsars	136.7 $^{+32}_{-29}$
M62Gaussian-NoPulsar	130.7 $^{+11}_{-12}$
M62Gaussian-WithPulsar	129.5 $^{+10}_{-10}$
M62-OnlyPulsars	239.2 $^{+41}_{-112}$

Table 5.3: Total numbers in BHs for different fits of M62 and  $1\sigma$  uncertainties.Figure 5.9: Posterior probability distribution of the  $f_{\text{BH}}$  in from all five fits discussed in this chapter and marked in the legend of the plot.

# Chapter 6

## Conclusions

This thesis is about the role of MSPs in constraining BHs in GCs and the effect of the number of MSPs with measured period derivatives on the uncertainties in the recovered BH mass fractions in the centre of GCs. To address this, we generated mock pulsar samples with period derivatives from a selected CMC model snapshot and fit multimass models to datasets with varying populations of MSPs. We also applied this method to fit mass models to observations of the globular cluster M62.

The main conclusions are given below:

1. The best-fitting model for the CMC6402-NoPULSARS mock dataset shows excellent agreement with the observational data, as detailed in Appendix B. This fit, which does not include pulsars, reveals no significant differences in model parameters or overall quality compared to best-fitting models of mock datasets that incorporate various numbers of pulsars with period derivatives. However, when examining the recovered black hole population, the CMC6402-NoPULSARS fit predicts a BH mass fraction of  $0.64_{-0.17}^{+0.22}\%$  ( $2471.7_{-683.3}^{+869.6} M_{\odot}$  BH mass) and estimates  $174_{-45}^{+55}$  BHs, both slightly lower than the true values from the CMC snapshot, which contains a BH mass fraction of 0.89% ( $3665.5 M_{\odot}$  BH mass) and 258 BHs. The absence of pulsar data doesn't degrade the overall fit and it leads to a slight underprediction of the cluster's dark remnant population within the uncertainty limit.

2. To better understand how BHs can be constrained in simulated globular clusters using methods applicable to real observations, we analyzed mock datasets different realizations incorporating 5, 10, and 25 pulsars with timing measurements. All the pulsars in the datasets had known spin periods and period derivatives, with approximately half also having orbital period and derivative measurements. The inclusion of pulsar data improved constraints on dark remnants in the cluster core and generally led to smaller uncertainties on the inferred BH mass fraction and better agreement with the true BH mass fraction (within uncertainties). Fits incorporating pulsar information predicted BH mass fractions closer to the true CMC snapshot value of 0.84%, with the improvement being particularly evident as more pulsars were included. Fits with 10 pulsars yielded BH mass fractions ranging from 0.17% to 1.48%, while those with 25 pulsars produced tighter constraints of ranging from 0.61% to 0.90%, demonstrating better agreement with the snapshot's true BH content. These results highlight how pulsar timing data can refine dynamical mass modeling, particularly for constraining the population of dark remnants in globular cluster cores.

3. We presented the results of fitting multimass dynamical models to observations of M62, including real pulsar timing data to constrain the mass distribution and BH population of this cluster, where we explored different priors for the heliocentric distance. We find that the M62GAUSSIAN-WITHPULSAR and M62GAUSSIAN-  
NoPULSAR models provide the best balance when fitting the stellar kinematic data and distance. Comparatively, the M62UNIFORM-NoPULSARS and M62UNIFORM-  
WITHPULSARS models, along with M62-ONLYPULSARS, slightly overestimate the LOS velocity dispersion profile. As shown in Figure 5.4 and Figure 5.6, these mod-

els requires a higher central mass concentration to account for all observed pulsars. Interestingly, the inclusion or exclusion of pulsar data did not significantly alter the overall fits or derived parameters under either distance prior. This suggests that the current pulsar sample may be too limited to further refine the black hole constraints when combined with existing stellar kinematics and datasets like the number density profile and stellar mass functions. Notably, our analysis finds no evidence supporting M62 as a core-collapsed cluster, contrary to previous claims in the literature (e.g. Djorgovski and Meylan, 1993). All of our model fits consistently indicate the presence of black hole mass in the cluster core, reinforcing this conclusion.

In the future, we plan to refine our understanding of BHs in GCs by fitting multimass models to a growing number of mock datasets with different realizations of millisecond MSPs with timing data. Furthermore, by conducting more fits with simulations of various clusters, we will be able to assess the reliability of our inferred uncertainties regarding black hole mass in GCs, based on mock MSP timing data. As we anticipate the discovery of more pulsars in GCs with upcoming radio telescopes, these techniques will assist us to use real pulsar timing data to probe GCs, offering valuable insights into dark remnants and mass distributions within these clusters.

# Appendix A

## M62 Pulsar Timing Data

Parameter	Models			
	A	C	D	E
$r[\text{arcmin}]$	0.32	0.19	0.15	0.06
DM	$114.98 \pm 0.04$	$114.55 \pm 0.05$	$114.23 \pm 0.02$	$113.79 \pm 0.02$
$P [\text{s}]$	$0.0052 \pm 2 \times 10^{-16}$	$0.0076 \pm 5 \times 10^{-16}$	$0.0034 \pm 2 \times 10^{-16}$	$0.0032 \pm 2 \times 10^{-17}$
$\dot{P} [\text{s/s}]$	$-1.3 \times 10^{-19} \pm 5 \times 10^{-25}$	$-6.3 \times 10^{-19} \pm 4 \times 10^{-25}$	$1.4 \times 10^{-19} \pm 3 \times 10^{-25}$	$3.1 \times 10^{-19} \pm 2 \times 10^{-25}$
$P_b [\text{s}]$	$3.3 \times 10^5 \pm 1.1 \times 10^{-4}$	$18576.01 \pm 6.91 \times 10^{-6}$	$96586.85 \pm 9.50 \times 10^{-6}$	$1.4 \times 10^4 \pm 2.6 \times 10^{-4}$
$\dot{P}_b [\text{s/s}]$	$-1.1 \times 10^{-6} \pm 2.6 \times 10^{-7}$	$-2.4 \times 10^{-8} \pm 1.6 \times 10^{-9}$	$2.9 \times 10^{-7} \pm 6.9 \times 10^{-8}$	—

Table A.1: Pulsar timing parameters with uncertainties for pulsars M62 A, C, D, and E. Values shown as median  $\pm$  uncertainty (([Vleeschower et al., 2024](#))).

Parameter	Models			
	F	G	H	I
$r[\text{arcmin}]$	0.07	0.23	0.42	0.07
DM	$113.29 \pm 0.02$	$113.67 \pm 0.03$	$114.70 \pm 0.03$	$113.35 \pm 0.02$
$P [\text{s}]$	$0.0022 \pm 2 \times 10^{-16}$	$0.0046 \pm 4 \times 10^{-16}$	$0.0037 \pm 2 \times 10^{-15}$	$0.0032 \pm 7 \times 10^{-16}$
$\dot{P} [\text{s/s}]$	$2.2 \times 10^{-19} \pm 2 \times 10^{-25}$	$-1.2 \times 10^{-19} \pm 2 \times 10^{-25}$	$3.8 \times 10^{-20} \pm 4 \times 10^{-23}$	$-3.4 \times 10^{-19} \pm 1 \times 10^{-25}$
$P_b [\text{s}]$	$1.8 \times 10^4 \pm 8.6 \times 10^{-6}$	$6.7 \times 10^4 \pm 8.6 \times 10^{-5}$	$1.12 \pm 8.7 \times 10^{-5}$	—
$\dot{P}_b [\text{s/s}]$	$1.1 \times 10^{-7} \pm 4.3 \times 10^{-9}$	—	—	$-6.1 \times 10^{-7} \pm 1.7 \times 10^{-7}$

Table A.2: Timing solutions for pulsars F, G, H, and I in M62. Values shown as median  $\pm$  uncertainty (([Vleeschower et al., 2024](#))).

## Appendix B

# Fits of the mock dataset with no pulsars CMC6402-NoPulsars

Parameter	Value
$W_0$	$2.95^{+0.14}_{-0.12}$
$M[10^6 M_\odot]$	$0.39^{+0.01}_{-0.01}$
$r_h[\text{pc}]$	$4.74^{+0.05}_{-0.05}$
$r_a$	$0.54^{+0.09}_{-0.09}$
$g$	$1.12^{+0.18}_{-0.15}$
$\delta$	$0.38^{+0.03}_{-0.04}$
$s_2$	$7.74^{+4.48}_{-3.71}$
$F$	$4.21^{+0.73}_{-0.63}$
$a_1$	$1.23^{+0.08}_{-0.07}$
$a_2$	$2.29^{+0.04}_{-0.06}$
$a_3$	$2.39^{+0.14}_{-0.07}$
$\text{BH}_{\text{ret}}[\%]$	$8.37^{+7.72}_{-3.23}$
$d[\text{kpc}]$	$8.85^{+0.12}_{-0.12}$

Table B.1: Best-fitting parameters with  $1\sigma$  uncertainty for CMC6402-NoPULSARS.

# Bibliography

F. Abbate, A. Possenti, A. Ridolfi, P. C. C. Freire, F. Camilo, R. N. Manchester, and N. D'Amico. Internal gas models and central black hole in 47 tucanae using millisecond pulsars. *Monthly Notices of the Royal Astronomical Society*, 2018.

Federico Abbate, Andrea Possenti, Monica Colpi, and Mario Spera. Evidence of nonluminous matter in the center of m62. *The Astrophysical Journal Letters*, 884(1):L9, 2019.

M. Ali Alpar and Jacob Shaham. Is gx5 – 1 a millisecond pulsar? *Nature*, 316(6025):239–241, Jul 1985.

Fabio Antonini and Mark Gieles. Merger rate of black hole binaries from globular clusters: theoretical error bars and comparison to gravitational wave data from gwtc-2. *Physical Review D*, 102(12):123016, 2020.

D. C. Backer, Shrinivas R. Kulkarni, Carl Heiles, M. M. Davis, and W. M. Goss. A millisecond pulsar. *Nature*, 300(5893):615–618, Dec 1982.

Manjari Bagchi. Luminosities of radio pulsars. *International Journal of Modern Physics D*, 22(10):1330021, 2013.

Andrés Bañares-Hernández, Francesca Calore, Jorge Martin Camalich, and Justin I Read. New constraints on the central mass contents of omega centauri from combined stellar kinematics and pulsar timing. *Astronomy & Astrophysics*, 693:A104, 2025.

Nate Bastian and Carmela Lardo. Globular cluster mass-loss in the context of multiple populations. *Monthly Notices of the Royal Astronomical Society*, 453(1):357–364, 2015.

Holger Baumgardt. N-body modelling of globular clusters: masses, mass-to-light ratios and intermediate-mass black holes. *Monthly Notices of the Royal Astronomical Society*, 464(2):2174–2202, 2017.

Holger Baumgardt, Vincent Henault-Brunet, Nolan Dickson, and Antonio Sollima. Evidence for a bottom-light initial mass function in massive star clusters. *Monthly Notices of the Royal Astronomical Society*, 521(3):3991–4008, 2023.

Holger Baumgardt and Eugene Vasiliev. Accurate distances to galactic globular clusters through a combination of gaia edr3, hst, and literature data. *Monthly Notices of the Royal Astronomical Society*, 505(4):5957–5977, 2021.

James Binney and Michael Merrifield. *Galactic Astronomy*, volume 62. Princeton University Press, 1998.

Jean P Brodie and Jay Strader. Extragalactic globular clusters and galaxy formation. *Annu. Rev. Astron. Astrophys.*, 44(1):193–267, 2006.

A. Corongiu, A. Possenti, A. G. Lyne, R. N. Manchester, F. Camilo, N. D’Amico, and J. M. Sarkissian. Timing of millisecond pulsars in ngc 6752 - ii. proper motions of the pulsars in the cluster outskirts. *The Astrophysical Journal*, 653:1417–1422, 2006.

T J L deBoer, M Gieles, E Balbinot, V Hénault-Brunet, A Sollima, L L Watkins, and I Claydon. Globular cluster number density profiles using gaia dr2. *Monthly Notices of the Royal Astronomical Society*, 485(4):4906–4935, 03 2019.

N Dickson, P Smith, V Hénault-Brunet, M Gieles, and H Baumgardt. Multimass modelling of milky way globular clusters – ii. present-day black hole populations. *Monthly Notices of the Royal Astronomical Society*, 529:331–347, 02 2024.

Nolan Dickson, Vincent Hénault-Brunet, Holger Baumgardt, Mark Gieles, and Peter J Smith. Multimass modelling of milky way globular clusters-i. implications on their stellar initial mass function above  $1 m\odot$ . *Monthly Notices of the Royal Astronomical Society*, 522(4):5320–5339, 2023.

S. Djorgovski and G. Meylan. Structure and dynamics of globular clusters. In S. G. Djorgovski and G. Meylan, editors, *Proceedings of a Workshop held in Berkeley, California, July 15-17, 1992, to Honor the 65th Birthday of Ivan King*, volume 50, page 325. Astronomical Society of the Pacific, 1993.

Aaron Dotter, Ata Sarajedini, and Jay Anderson. Globular clusters in the outer galactic halo: New hubble space telescope/advanced camera for surveys imaging of six globular clusters and the galactic globular cluster age–metallicity relation\*. *The Astrophysical Journal*, 738(1):74, aug 2011.

Duncan A. Forbes, Nate Bastian, Mark Gieles, Robert A. Crain, J. M. Diederik Kruijssen, Søren S. Larsen, Sylvia Ploeckinger, Oscar Agertz, Michele Trenti, Annette M. N. Ferguson, Joel Pfeffer, and Oleg Y. Gnedin. Globular cluster formation and evolution in the context of cosmological galaxy assembly: open questions. *Royal Society*, volume 474, 2018.

P. Freire. Pulsars in globular clusters, 2010. Accessed: 2025-01-27.

P. C. C. Freire, A. Ridolfi, M. Kramer, C. Jordan, R. N. Manchester, P. Torne, J. Sarkissian, C. O. Heinke, N. D’Amico, F. Camilo, D. R. Lorimer, and A. G. Lyne. Long-term observations of the pulsars in 47 tucanae – ii. proper motions, accelerations and jerks. *Monthly Notices of the Royal Astronomical Society*, 471(1):857–876, 06 2017.

Mark Gieles, Eduardo Balbinot, Rashid I. S. M. Yaaqib, Vincent Hénault-Brunet, Alice Zocchi, Miklos Peuten, and Peter G. Jonker. Mass models of ngc 6624 without an intermediate-mass black hole. *Monthly Notices of the Royal Astronomical Society*, 473(4):4832–4839, 10 2017.

Mark Gieles and Alice Zocchi. A family of lowered isothermal models. *Monthly Notices of the Royal Astronomical Society*, 454(1):576–592, 2015.

Mirek Giersz, Douglas C Heggie, Jarrod R Hurley, and Arkadiusz Hypki. Mocca code for star cluster simulations–ii. comparison with n-body simulations. *Monthly Notices of the Royal Astronomical Society*, 431(3):2184–2199, 2013.

Raffaele Gratton, Angela Bragaglia, Eugenio Carretta, Valentina D’Orazi, Sara Lucatello, and Antonio Sollima. What is a globular cluster? an observational perspective. *The Astronomy and Astrophysics Review*, 27(1):8, 2019.

J. E. Grindlay and C. D. Bailyn. Birth of millisecond pulsars in globular clusters. *Nature*, 336(6194):48–50, Nov 1988.

Douglas Heggie and Piet Hut. *The Gravitational Million-Body Problem*. Cambridge University Press, 01 2003.

Vincent Hénault-Brunet, Mark Gieles, Jay Strader, Miklos Peuten, Eduardo Balbinot, and Kaela EK Douglas. On the black hole content and initial mass function of 47 tuc. *Monthly Notices of the Royal Astronomical Society*, 491(1):113–128, 2020.

M. Hénon. The monte carlo method. *International Astronomical Union Colloquium*, 10:151–167, 1971.

V Hénault-Brunet, M Gieles, A Sollima, L L Watkins, A Zocchi, I Claydon, E Pancino, and H Baumgardt. Mass modelling globular clusters in the gaiaera: a method comparison using mock data from an n-body simulation of m 4. *Monthly Notices of the Royal Astronomical Society*, 483(1):1400–1425, 11 2019.

V Hénault-Brunet, M Gieles, J Strader, M Peuten, E Balbinot, and K E K Douglas. On the black hole content and initial mass function of 47 tuc. *Monthly Notices of the Royal Astronomical Society*, 491(1):113–128, 10 2020.

Kyle Kremer, S Ye Claire, Nicholas Z Rui, Newlin C Weatherford, Sourav Chatterjee, Giacomo Fragione, Carl L Rodriguez, Mario Spera, and Frederic A Rasio. Modeling dense star clusters in the milky way and beyond with the cmc cluster catalog. *The Astrophysical Journal Supplement Series*, 247(2):48, 2020.

Kyle Kremer, Wenbin Lu, Carl L. Rodriguez, Mitchell Lachat, and Frederic A. Rasio. Tidal disruptions of stars by black hole remnants in dense star clusters. *The Astrophysical Journal*, 881(1):75, aug 2019.

- A. D. Mackey, M. I. Wilkinson, M. B. Davies, and G. F. Gilmore. Black holes and core expansion in massive star clusters. *Monthly Notices of the Royal Astronomical Society*, 386(1):65–95, 03 2008.
- RN Manchester. Millisecond pulsars, their evolution and applications. *Journal of Astrophysics and Astronomy*, 38(3):42, 2017.
- Kwangmin Oh, C Y Hui, K L Li, and A K H Kong. Multi-epoch x-ray imaging of globular cluster m62 with chandra. *Monthly Notices of the Royal Astronomical Society*, 498(1):292–303, 08 2020.
- Bharath Pappabiraman, Stefan Umbreit, Wei-keng Liao, Alok Choudhary, Vassiliki Kalogera, Gokhan Memik, and Frederic A. Rasio. A parallel monte carlo code for simulating collisional n-body systems. *The Astrophysical Journal Supplement Series*, 204(2):15, jan 2013.
- BBP Perera, BW Stappers, AG Lyne, CG Bassa, Ismaël Cognard, Lucas Guillemot, Michael Kramer, Gilles Theureau, and Grégory Desvignes. Evidence for an intermediate-mass black hole in the globular cluster ngc 6624. *Monthly Notices of the Royal Astronomical Society*, 468(2):2114–2127, 2017.
- M. Peuten, A. Zocchi, M. Gieles, A. Gualandris, and V. Hénault-Brunet. A stellar-mass black hole population in the globular cluster ngc 6101? *Monthly Notices of the Royal Astronomical Society*, 462(3):2333–2342, 09 2016.
- E. S. Phinney and B. M. S. Hansen. The pulsar planet production process. In J. A. Phillips, Steve E. Thorsett, and Shri R. Kulkarni, editors, *Planets Around Pulsars*, volume 36 of *Astronomical Society of the Pacific Conference Series*, pages 371–390, January 1993.
- Brian J. Prager, Scott M. Ransom, Paulo C. C. Freire, Jason W. T. Hessels, Ingrid H. Stairs, Phil Arras, and Mario Cadelano. Using long-term millisecond pulsar timing to obtain physical characteristics of the bulge globular cluster terzan 5. *The Astrophysical Journal*, 845(2):148, aug 2017.
- Adrian M. Price-Whelan, Semyeong Oh, and David N. Spergel. Spectroscopic confirmation of very-wide stellar binaries and large-separation comoving pairs from gaia dr1. *The Journal of Open Source Software*, 2017.
- Alvio Renzini. Finding forming globular clusters at high redshifts. *Monthly Notices of the Royal Astronomical Society: Letters*, 469(1):L63–L67, 04 2017.
- Carl L. Rodriguez, Newlin C. Weatherford, Scott C. Coughlin, Pau Amaro-Seoane, Katelyn Breivik, Sourav Chatterjee, Giacomo Fragione, Fulya Kiroğlu, Kyle Kremer, Nicholas Z. Rui, Claire S. Ye, Michael Zevin, and Frederic A. Rasio. Modeling dense star clusters in the milky way and beyond with the cluster monte carlo code. *The Astrophysical Journal Supplement Series*, 258(2):22, jan 2022.

Nicholas Z. Rui, Kyle Kremer, Newlin C. Weatherford, Sourav Chatterjee, Frederic A. Rasio, Carl L. Rodriguez, and Claire S. Ye. Missing title placeholder. *Missing Journal Placeholder*, 2021.

I. S. Shklovskii. The effect of the proper motion of pulsars on the observed period variation. *Soviet Astronomy*, 13:562, 1970.

Peter J. Smith, Vincent Hénault-Brunet, Nolan Dickson, Mark Gieles, and Holger Baumgardt. Probing populations of dark stellar remnants in the globular clusters 47 tuc and terzan 5 using pulsar timing. *The Astrophysical Journal*, 975(2):268, nov 2024.

Joshua S Speagle. dynesty: a dynamic nested sampling package for estimating bayesian posteriors and evidences. *Monthly Notices of the Royal Astronomical Society*, 493(3):3132–3158, 02 2020.

G. Srinivasan. Recycled pulsars. *New Astronomy Reviews*, 54(3):93–100, 2010. Proceedings: A Life With Stars.

L Vleeschower, A Corongiu, BW Stappers, PCC Freire, A Ridolfi, F Abbate, SM Ransom, A Possenti, PV Padmanabh, V Balakrishnan, et al. Discoveries and timing of pulsars in m62. *Monthly Notices of the Royal Astronomical Society*, 530(2):1436–1456, 2024.

Li-Chun Wang and Yi Xie. Probing dark contents in globular clusters with timing effects of pulsar acceleration. *Research in Astronomy and Astrophysics*, 21(11):270, 2021.